

The n-capture and α -elements abundance ratios scatter in old stellar populations. Cosmological simulations of the stellar halo

Cecilia Scannapieco^{1,2}, Gabriele Cescutti^{3,4} and Cristina Chiappini⁵

¹ *Universidad de Buenos Aires, Facultad de Ciencias Exactas y Naturales, Departamento de Física, Buenos Aires, Argentina*

² *CONICET, Buenos Aires, Argentina*

³ *INAF, Osservatorio Astronomico di Trieste, Via G.B. Tiepolo 11, 34143, Trieste, Italy;*

⁴ *IFPU-Institute for Fundamental Physics of the Universe, Via Beirut 2, 34014, Trieste, Italy*

⁵ *Leibniz-Institut für Astrophysik Potsdam (AIP), An der Sternwarte 16, D-14482, Potsdam, Germany*

Accepted 14 July 2021 Received ...; in original form ...

ABSTRACT

We investigate the origin of the abundance ratios and scatter of α - and neutron-capture elements of old, metal-poor stars, using hydrodynamical simulations of galaxy formation in a cosmological context. For this, we implement a novel treatment for the production and distribution of chemical products of Type II supernovae, which considers, on one side, the effects of the rotation of massive stars on the chemical yields and, on the other hand, the effects of the different life-times of stars that are progenitors of this type of supernovae. We first describe and test our implementation on idealized initial conditions of an isolated galaxy, and then focus on the stellar halo of a Milky Way-mass galaxy simulated in a cosmological context, studying the abundances and scatter of [O/Fe], [Mg/Fe], [Si/Fe], [Sr/Fe], [Eu/Fe] and [Ba/Fe]. Our model is able, for the first time in a cosmological simulation, to describe *at the same time* the low scatter in the abundances of α -elements and the higher scatter associated to neutron-capture elements in the halo stars, as suggested by observations of the Milky Way. We also reproduce the scatter observed in the [Sr/Ba] ratio, which is a direct consequence of the treatment of the fast-rotating stars and the dependence of the chemical yields on the metallicity, mass and rotational velocities. Our simulations show that such scatter patterns appear naturally if the difference life-times of stars of different mass – and therefore the time of their ejection – are properly described, without the need to invoke for additional mixing mechanisms or a distinct treatment of the α - and neutron-capture elements. Our results show that simulations of this type will help characterizing and identifying the past accretion debris as well as the pristine in-situ populations in the Galaxy unveiled by Gaia and spectroscopic data.

Key words: galaxies: formation - galaxies: abundances - galaxies: evolution - methods: numerical - cosmology: theory

1 INTRODUCTION

Thanks to the Gaia satellite which provides precise measurements of parallax and proper-motion of stars (Gaia Collaboration, Brown et al. 2021 and references therein), as well as spectroscopic information coming from major surveys (complementing the Gaia data with radial velocities and chemistry), the complexity of the formation history of our Galaxy has become evident. In particular, the local low-metallicity regime (below [Fe/H] ~ -0.8) turns out to be made of a collection of debris from past impacts with smaller galaxies (Helmi 2020 and references therein) as well as early in-situ formed stars (Miglio et al. 2021; Montalbán et al. 2021 - usually more enhanced in α -elements).

The most important past accretion event in the early history of the Milky Way seems to have been the merger with Gaia-Enceladus (Helmi et al. 2018; Belokurov et al. 2018). This event could be confirmed thanks to the combination of Gaia DR2 (Gaia Collaboration, Brown et al. 2018) and APOGEE (Majewski et al. 2017) data. The discovery and characterization of other debris is a very active field and the several large spectroscopic surveys are playing a key role (e.g. Koppelman et al. 2019; Myeong et al. 2019; Naidu et al. 2020; Re Fiorentin et al. 2021). Indeed, the information brought by detailed chemical abundances is of paramount importance in the identification of a star’s origin.

In particular, the role of n-capture elements in this con-

text, although not yet fully explored in cosmological simulations, is certainly going to be central as suggested by recent observational results (see for instance [Aguado et al. 2021](#); [Limberg et al. 2021](#); [Gudin et al. 2021](#); [Gull et al. 2021](#)). Among metal-poor stars it is known that abundance ratios involving n-capture elements do show a large spread (e.g. [François et al. 2007](#); [Montes et al. 2007](#)). This is a consequence of the strong dependency of the stellar yields of these elements on the stellar mass and on different production channels (e.g. massive stars or neutron-star mergers). Hence, the study of the scatter among two different n-capture elements can bring important insights both on stellar nucleosynthesis and galaxy assembly (e.g. [Cescutti et al. 2013](#); [Cescutti & Chiappini 2014](#); [Wehmeyer et al. 2015](#); [Wehmeyer et al. 2019](#); [Brauer et al. 2020](#); see also review by [Cowan et al. 2021](#) and references therein). The fast observational progress in this area urgently calls for informative theoretical models which help the interpretation of chemo-kinematic datasets (with 6D phase space information plus chemistry and, sometimes, age - [Valentini et al. 2019](#); [Montalbán et al. 2021](#); [Miglio et al. 2021](#)).

The use of n-capture elements brings at least two important difficulties that have to be addressed before model predictions including these elements can become useful. The first is the uncertainties in the nucleosynthetic sites of production (in particular in the case of r-process elements, but also related to the early contribution of massive stars for the s-process - e.g. [Choplin et al. 2018](#) and references therein). The second difficulty is related to the implementation of the evolution of these elements in cosmological simulations, and possible resolution/mixing effects that can affect their predictions (e.g. [Shen et al. 2015](#); [van de Voort et al. 2015](#); [Naiman et al. 2018](#); [Haynes & Kobayashi 2019](#); [van de Voort et al. 2020](#)). Most of these previous work consider only the production of elements by r-process events, either on-the-fly or in post-processing, or analyse the evolution of Eu only. In this work, we implement a detailed chemical enrichment model which includes the production and distribution of Sr, Ba and Eu in a cosmological simulation. In particular, we explore the dispersion in light to heavy neutron-capture elements considering both r-process events and the contribution of massive stars with an s-process production ([Frischknecht et al. 2016b](#); [Limongi & Chieffi 2018](#); [Choplin et al. 2018](#)). As summarized in [Chiappini \(2013\)](#), the impact of spinstars in the chemical enrichment of the earliest phases of our Galaxy is not confined to carbon and nitrogen ([Chiappini et al. 2006, 2008](#); [Prantzos et al. 2018](#)), but extends to s-process elements as well ([Pignatari et al. 2008](#); [Chiappini et al. 2011](#)). As a first step, in previous works we studied the scatter in n-capture abundance ratios using stochastic inhomogeneous chemical evolution models ([Cescutti et al. 2013](#); [Cescutti & Chiappini 2014](#); [Cescutti et al. 2015](#)). Such models, by construction, do not include accretion of stars formed in smaller galaxies as we know to be the case in the Milky Way. Here we will investigate the impact of accretion events and the cosmological growth of halos on these previous results, in a the context of the Λ -Cold Dark Matter model.

This paper is organized as follows. In Section 2 we describe our new model for chemical enrichment and present various numerical tests to our implementation, including simulations using idealized and cosmological initial condi-

tions for galaxy formation. Section 3 discusses the abundances and scatter of neutron-capture and α -elements for the stellar halo obtained in our cosmological simulations, and in Section 4 we present our conclusions.

2 THE SIMULATIONS

2.1 Numerical Implementation

We employ for this study the cosmological, hydrodynamical, Smoothed Particle Hydrodynamics (SPH) code GADGET3 ([Springel et al. 2008](#)), with the updates of [Scannapieco et al. \(2005, 2006\)](#). This model follows the evolution of dark and baryonic matter in the context of the standard cosmological model, including sophisticated recipes for star formation, chemical enrichment, supernova feedback, and metal-dependent cooling. For this project, we have modified our standard code, to which we refer to as the CS model, in order to properly describe the early enrichment phases of the interstellar medium, therefore allowing for a detailed study of the chemical abundances of the very old stars in galaxies. In the following subsections, we describe the CS model in terms of the physical modules relevant for this study, the updates we have implemented to the chemical routines, the chemical species and yields that we adopt, and the setup of the simulations presented in this work. These modifications are easy to implement in more recent and future simulations by the community.

2.1.1 Star formation, feedback and chemical enrichment in the CS model

In the CS model, star particles form according to the Kennicutt-Schmidt law ([Kennicutt 1998](#)), in a stochastic manner ([Springel & Hernquist 2003](#)). Gas particles are eligible for star formation if they are denser than a critical value (ρ_c) and are in a convergent flow. For these particles, the star formation rate (SFR) per unit volume is

$$\rho_{\text{SFR}} = c_* \frac{\rho}{\tau_{\text{dyn}}} \quad (1)$$

where c_* is a star formation efficiency, ρ is the gas density and $\tau_{\text{dyn}} = (4\pi G\rho)^{-1/2}$ the dynamical time of the particle. Once formed, star particles are treated as single stellar populations (SSP) with a given Initial Mass Function (IMF), and return metals and energy to their surroundings during supernova (SN) explosions. As the interstellar medium (ISM) gets polluted, new stars are produced with higher metallicities, because star particles inherit the element abundances of the gas from which they form.

Our model includes treatments for chemical enrichment and energy feedback originated in Type II (SNII) and Type Ia (SNIa) events, based on assumptions for their rates, chemical yields and explosion times¹. When a star explodes as

¹ We refer the interested reader to [Scannapieco et al. \(2005\)](#) for details on these assumptions; we note, however, that in some cases they have been modified for this work, as we describe in the next subsection.

SNII or SNIa, the associated chemical production is distributed into its N_{Ngb} gas neighbours, in proportions given by the SPH kernel.

The CS model is based on a multiphase gas treatment which allows coexistence of dense and diffuse phases in the same spatial region; in this context, exploding stars will have well-defined hot and cold neighbours. We assume that both types of SNe eject the same amount of energy E_{SN} to the ISM, which is distributed in equal proportions to the local cold and hot gas phases of the exploding stars. Energy feedback into hot neighbors occurs at the time of explosion; however, for cold neighbors energy from successive explosions is instead accumulated and deposited only after a time-delay which depends on the local conditions of the cold and hot gas phases, as described in Scannapieco et al. (2006). In this way, artificial loss of SN energy in high-density regions is prevented. Gas cooling is described using the metal-dependent tables of Sutherland & Dopita (1993).

The CS model has been shown to be successful in producing galaxies similar to those observed, both in the case of Milky Way (MW) mass galaxies (Scannapieco et al. 2008, 2009, 2010, 2011; Tissera et al. 2013; Nuza et al. 2014; Tissera et al. 2014) and in dwarf systems (Sawala et al. 2010, 2011, 2012). In particular, our SN feedback model is able to reproduce the formation of disks from cosmological initial conditions (Scannapieco et al. 2008, 2009), and to produce galaxies that are in general terms consistent with observations of the galaxy population (Scannapieco et al. 2012; Guidi et al. 2016).

2.1.2 Implementing multiple explosion times for SNII

In the CS model, each star particle, which represents a SSP with given age, metallicity and IMF, explodes as SNII in a single event. The time of the explosion (i.e. the time at which the SN ejecta is injected into the surrounding gas particles) is determined by the mean age of the individual stars of the SSP, which we calculate following Raiteri et al. (1996) who provides (mass and metallicity-dependent) life-time estimations based on the theoretical stellar tracks of the Padova group (Bertelli et al. 1994). Each star particle “explodes” as SNII in a single event; therefore, the most and least massive stars of the SSP it represents eject their chemical products simultaneously. This assumption allows to describe the overall evolution of chemical abundances in galaxies; however, it does not properly describe the first stages of enrichment of the ISM, which will be enriched gradually, starting with the most massive, most short-lived stars. Such a gradual enrichment will leave imprints in the chemical properties of the very old, metal-poor stars, as stars of different mass will contribute chemical material of different nature (e.g. end-products of r- vs s-processes vs α -elements) at different times. It will also significantly affect the spread in chemical abundances, which we investigate in this work.

In order to better describe the enrichment of the ISM occurring in short time-scales, we have modified our code such that each SNII event is represented by a series of different “explosions”, which we chose to best describe the enrichment of the different chemical elements we are interested in (see next subsection). In our new model, we assume that each star particle will experience 5 different explosion events, which occur at 30, 18, 9, 6 and 3 Myr from its formation.

These correspond to stars in the mass ranges [8-9), [9,14), [14, 27.5), [27.5, 45) and [45-100] M_{\odot} , respectively, according to the estimations of Maeder & Meynet (1989)².

2.1.3 Chemical species and yields

As in this paper we are mainly interested in the early phases of chemical enrichment, we consider only the nucleosynthesis of the massive stars, that are the main drivers of the pollution of the ISM in this first enrichment period. In particular, we consider the nucleosynthesis of massive stars in terms of the following chemical species: H, He, C, N, O, Fe, Mg, Si, Ba, Eu, Sr and Y. The corresponding yields are parameterized in terms of 5 metallicity ranges, separated by $Z = 0, 0.0001 Z_{\odot}, 0.01 Z_{\odot}, 0.1 Z_{\odot}$ and Z_{\odot} .

For He, C, N, O, Mg and Fe, we have adopted the same nucleosynthesis than the ones used in Chiappini et al. (2006, 2008) and Cescutti & Chiappini (2010). The nucleosynthesis of the light elements is metal-dependent and based on the work of the Geneva group (Meynet & Maeder 2002; Hirschi 2007). The novelty of these works is that they considered the impact of rotation in massive stars at low metallicity, and the rotation changes the final enrichment of the light elements, in particular of nitrogen. In the case of Mg, Si and Fe, we consider yields, from the work of Woosley & Weaver (1995), slightly modified (see François et al. 2004) to best match the averaged trend of extremely metal-poor stars measured by Cayrel et al. (2004).

For the nucleosynthesis of the neutron capture elements, we assume an r-process contribution as the one adopted in Cescutti et al. (2013): a strong production in a narrow mass range of 8 – 10 M_{\odot} that we call standard r-process site. These yields have been chosen to reproduce the mean trend of [Ba/Fe] versus [Fe/H] using the homogeneous chemical evolution model of Chiappini et al. (2006). For the remaining neutron capture elements, we scale the r-process contribution using the ratios observed in r-process rich stars (Snedden et al. 2008). We also adopt an s-process contribution coming from rotating massive stars, using the yields computed in Frischknecht et al. (2016a). Among the set of models, we have adopted a robust production of s-process elements, achieved by considering s-process yields of massive stars for $v_{\text{ini}}/v_{\text{crit}} = 0.5$ (fast rotators) and for a reaction rate $^{17}\text{O}(\alpha, \gamma)^{21}\text{Ne}$ one tenth of Caughlan & Fowler (1988); current uncertainties on this rate are still large.

The stellar yields adopted here are essentially the same as the ones adopted in our non-cosmological stochastic model presented in Cescutti & Chiappini (2014). Using similar prescriptions, now applied to cosmological simulations, allows to test the impact of complex merger histories on the interpretation of the observed abundance scatter of different chemical elements, which is one of the main goals of the present work.

Throughout this paper, we have assumed the solar abundances given by Grevesse et al. (2010).

² Note that although small differences in the lifetimes estimations are expected for different stellar models (e.g. the Geneva ones), these will not affect our results as the differences are smaller than the grid of explosion times considered here.

2.1.4 Simulation set-up

As we describe in the next Sections, we have tested our code in idealized simulations of the evolution of an isolated galaxy, as well as in simulations in a cosmological context. In order to facilitate comparison, we have kept the same input parameters for star formation, chemical enrichment and feedback in all runs, and performed simulations with the CS standard code and with the new implementation. We have assumed a star formation efficiency of $c_* = 0.1$, a star formation threshold of $\rho_c = 0.1 \text{ cm}^{-3}$, and $E_{\text{SN}} = 0.7 \times 10^{51}$ erg of energy per SN. These choices for the input parameters produce galaxies with realistic disk sizes (Scannapieco et al. 2008).

Furthermore, as we are interested in the old stellar component, we have switched off our model to include SNIa explosions, which will allow us to better isolate the effects of the new implementation on the simulated galaxies, and we also ignore the effects of AGB stars. Finally, in order to facilitate comparison with the results of the galactic chemical evolution models of Cescutti et al. (2013), we have assumed a Scalo IMF. In future papers, we will explore the impact of SNIa and AGBs in the earliest phases of the chemical enrichment, but this is beyond the scope of the present work. However, we have run some tests that have confirmed the impact of the latter to be negligible in our results, when standard stellar yields are adopted.

2.2 Tests I - Isolated galaxy simulations

In order to test our implementation of multiple explosions per SN event, we first carried out a set of idealized simulations of isolated disc galaxies. We run two simulations using these initial conditions, that are identical except for the number of events associated to SNII explosions (N_{SNII}) per star particle: $N_{\text{SNII}} = 1$ (as in the standard CS model) or $N_{\text{SNII}} = 5$ (Sec. 2.1.2). We will refer to them as the “SE64” and “ME64” runs, respectively³. In order to test possible dependencies of our results on numerical choices we have run additional simulations varying the number of particles (Appendix A1), as well as the number of SPH neighbours, which sets the smoothing region, i.e. radius over which the chemical elements ejected in SN explosions are distributed (Appendix A2). Table 1 summarizes the main properties of the different simulations analysed in this work.

2.2.1 Initial conditions

The initial conditions used in this Section are generated by radially perturbing a spherical grid of superposed dark matter and gas particles to produce a cloud with density profile $\rho(r) \sim r^{-1}$, as in Navarro & White (1993). The sphere is initially in solid body rotation with an angular momentum characterized by spin parameter $\lambda \simeq 0.1$, and the gas is cold (i.e. the initial thermal energy is only 5 per cent of its binding energy). The simulated system has a total mass of $10^{12} M_\odot$, 10 per cent of which is in the form of baryons, and the initial radius is 100kpc. Our fiducial tests used $N_{\text{tot}} = 2 \times 64^3$

³ The number “64” encodes information on the number of particles of the simulation, see Appendix A1.

particles initially⁴, yielding particle masses of $6.55 \times 10^6 M_\odot$ and $7.28 \times 10^5 M_\odot$ for dark matter and gas (Table 1), respectively, and we adopted a gravitational softening length of 350 pc for all particles. The simulations of this Section were run for 2 Gyr, although we focus our analysis on the early phases of the formation of the galaxies, before the first Gyr of evolution.

We note that the idealized initial conditions of this Section yield a simple model for disc formation, which is an ideal test bench for the performance and validity of the code. However, these models are not meant to provide a realistic scenario for the whole galaxy formation process, in particular because there is no gas infall which, in a cosmological context, has important effects on the growth and evolution of a galaxy. In Section 2.3, we run and analyse simulations of the formation of a Milky-Way mass galaxy in full cosmological context.

2.2.2 Star formation and chemical evolution

Our implementation of multiple events per SN explosion is expected to affect not only the chemical properties of the galaxies but also the star formation process, as the rate at which the gas is enriched will impact the cooling rates, affecting the amount of cold/dense gas available for star formation at different times. This will produce an initial change in the star formation rate due to variations in the enrichment level, and further changes due to the variations in the amount of available feedback⁵.

Fig. 1 shows the star formation rate (SFR), and the evolution of the stellar mass (M_{star}) and metallicity (Z) in simulations SE64 and ME64. The two simulations have similar SFRs and integrated stellar masses during the first ~ 0.5 Gyr; however, the metallicity of the stellar population is clearly distinct from very early times. This difference originates in the variations of the enrichment of the ISM in the two runs: in ME64 the first explosion events associated to the most massive short-lived stars occur very quickly after star formation (i.e. 3 Myr, Section 2.1.2) triggering a very fast enrichment of the surrounding gas. In contrast, in SE64 the single explosion associated to all SNII within a star particle occurs after $\sim 15 - 20$ Myr from its formation⁶.

The differences in the early chemical pollution of the ISM in our two simulations can be seen in Fig. 2, where we compare the gas metallicities, in terms of the [Fe/H] abundance, for simulations SE64 and ME64, and for various times between 0.1 and 0.35 Gyr. Even though star formation starts at the same time in both simulations, in ME64 the enrichment of the ISM is faster compared to SE64, particularly during the first 200 Myr after star formation begins. At later times, the differences dilute, as both the 5 explosion

⁴ Note that the total number of particles changes with time, as each gas particle can produce a maximum of two stars.

⁵ We note that these effects might be enhanced/reduced in the simulations analysed in this Section due to the idealized nature of the ICs (see Section 2.3 for simulations in a cosmological context).

⁶ Note that the time of the explosion of star particles associated to SNII in the CS model is the mean age of the individual stars within a star particle that are progenitors of SNII (Section 2.1.2). The explosion time changes from particle to particle, and depends on the choice of the IMF and the metallicity of the star particle.

Table 1. Main characteristics of the simulations used in this work: reference name, type of initial conditions, number of events assumed per SNI (N_{SNI}), total number of particles of the simulation (N_{tot}), assumed number of SPH neighbours (N_{Ngb}), reference Section, and masses of the dark matter (m_{DM}) and baryonic (m_{bar}) particles.

Name	Initial Conditions	N_{SNI}	N_{tot}^1	N_{Ngb}	Section	m_{DM} [M_{\odot}]	m_{bar} [M_{\odot}]
SE64	Isolated	1	2×64^3	40	2.2	6.55×10^6	7.28×10^5
ME64	Isolated	5	2×64^3	40	2.2	6.55×10^6	7.28×10^5
SE64- $N_{\text{Ngb}64}$	Isolated	1	2×64^3	64	A2	6.55×10^6	7.28×10^5
ME64- $N_{\text{Ngb}64}$	Isolated	5	2×64^3	64	A2	6.55×10^6	7.28×10^5
SE64- $N_{\text{Ngb}128}$	Isolated	1	2×64^3	128	A2	6.55×10^6	7.28×10^5
ME64- $N_{\text{Ngb}128}$	Isolated	5	2×64^3	128	A2	6.55×10^6	7.28×10^5
SE32	Isolated	1	2×32^3	40	A1	5.22×10^7	5.80×10^6
ME32	Isolated	5	2×32^3	40	A1	5.22×10^7	5.80×10^6
SE32- $N_{\text{Ngb}64}$	Isolated	1	2×32^3	64	A2	5.22×10^7	5.80×10^6
ME32- $N_{\text{Ngb}64}$	Isolated	5	2×32^3	64	A2	5.22×10^7	5.80×10^6
SE32- $N_{\text{Ngb}128}$	Isolated	1	2×32^3	128	A2	5.22×10^7	5.80×10^6
ME32- $N_{\text{Ngb}128}$	Isolated	5	2×32^3	128	A2	5.22×10^7	5.80×10^6
SE128	Isolated	1	2×128^3	40	A1	8.19×10^5	9.10×10^4
ME128	Isolated	5	2×128^3	40	A1	8.19×10^5	9.10×10^4
SE128- $N_{\text{Ngb}64}$	Isolated	1	2×128^3	64	A2	8.19×10^5	9.10×10^4
ME128- $N_{\text{Ngb}64}$	Isolated	5	2×128^3	64	A2	8.19×10^5	9.10×10^4
SE128- $N_{\text{Ngb}128}$	Isolated	1	2×128^3	128	A2	8.19×10^5	9.10×10^4
ME128- $N_{\text{Ngb}128}$	Isolated	5	2×128^3	128	A2	8.19×10^5	9.10×10^4
SE	Cosmological	1	1854223	40	2.3	2.16×10^6	4.11×10^5
ME	Cosmological	5	1608991	40	2.3	2.16×10^6	4.11×10^5

¹ In the case of the cosmological simulations N_{tot} refers to the total number of particles within the virial radius of the galaxy at the end of the simulation ($z = 0$).

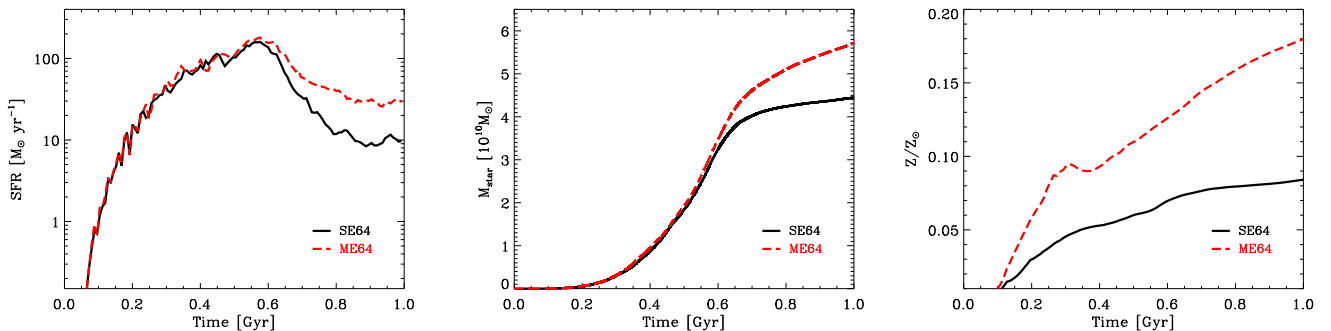


Figure 1. Star formation rate, cumulative stellar mass and total stellar metallicity, as a function of time, for our simulations SE64 and ME64.

events in ME64 and the single event in SE64 have occurred, and the accumulated chemical production has been released. As a result, the predicted number of very metal-poor stars formed within the first 200 Myr when considering the multi-explosion scenario is systematically smaller than when assuming that all core-collapse SNe contributed at a single time.

The differences in the very early epochs, *can thus* leave clear imprints in the galaxies, both in the enrichment levels of the stellar and gaseous components (higher stellar metallicities in ME64 compared to SE64) and in the cooling rates (enhanced cooling in ME64 due to the faster enrichment). As a result, the star formation rates in ME64 are higher. As

a result, after 1 Gyr of evolution the stellar mass is $\sim 30\%$ higher in ME64 compared to SE64, and the stellar metallicity is about 2 times higher (Fig. 1).

Fig. 3 shows the distribution functions of stellar [Fe/H] abundances for simulations SE64 and ME64, after 0.25, 0.5 and 1 Gyr of evolution. From these plots we can observe that, following the characteristics of the ISM enrichment, the differences in the [Fe/H] distributions in models SE64 and ME64 are more important at early times, both for low and high metallicity. The distributions are less dissimilar at later times; however, the differences originated early on on the stellar abundances can still be seen after 1 Gyr of evolution.

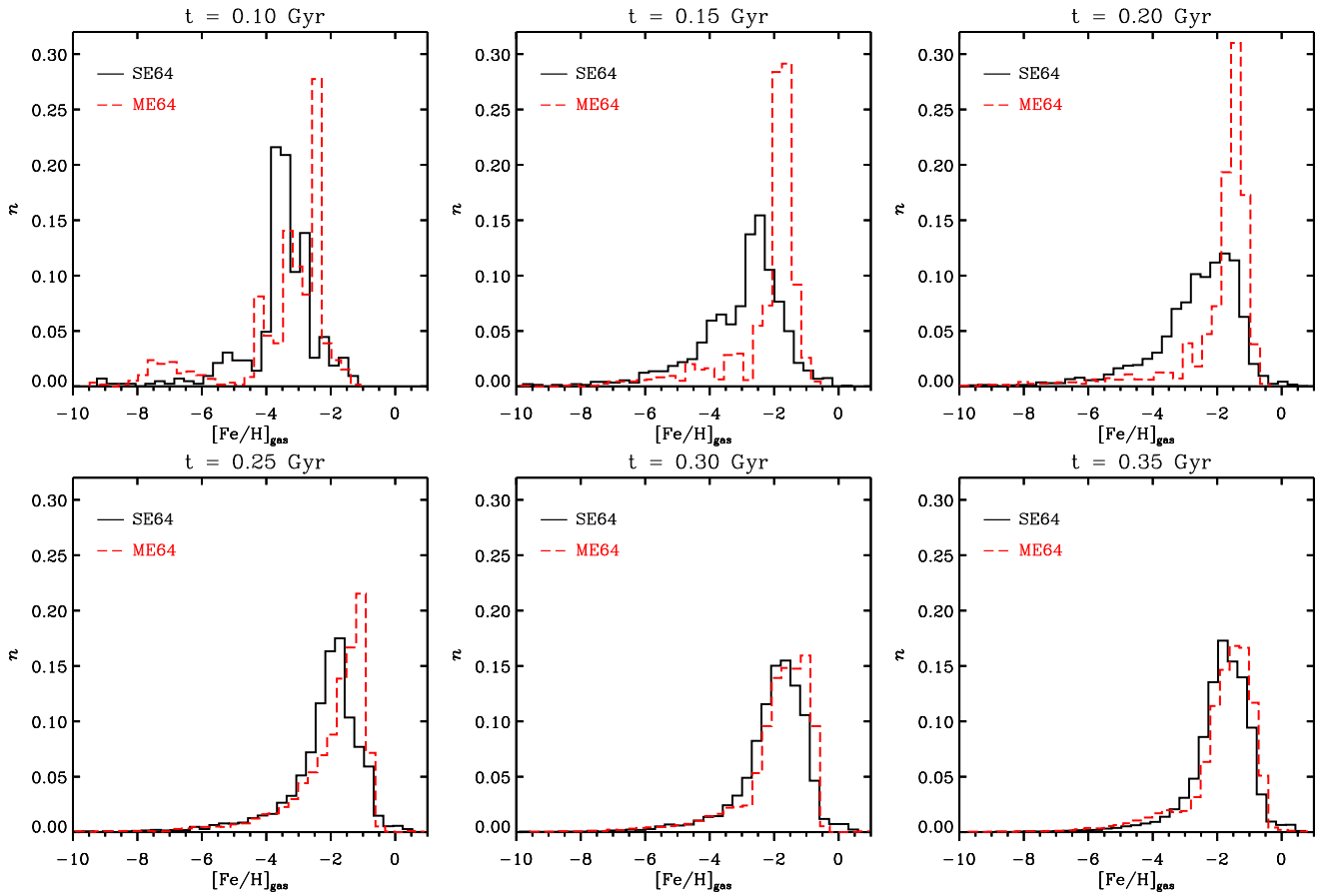


Figure 2. Distribution of $[\text{Fe}/\text{H}]$ for the gas in simulations SE64 and ME64, for various times during the early enrichment phases.

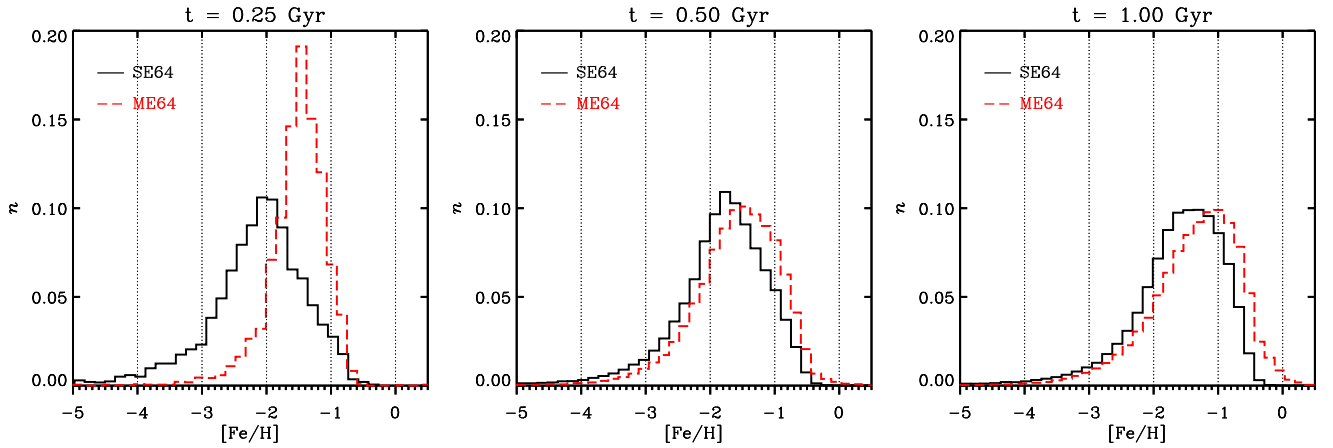


Figure 3. Distribution of the stellar $[\text{Fe}/\text{H}]$ for simulations SE64 and M64 at different times of the simulation: 0.25 Gyr, 0.5 Gyr and 1 Gyr.

As explained above, imprints of the differences in the early chemical pollution of the ISM in runs SE64 and ME64 appear in the chemical properties of the stars. This is important given that, if properly interpreted, observations of the stellar population of a galaxy could allow to reconstruct the level of enrichment of the ISM at different times, information that is otherwise inaccessible.

2.2.3 Element ratios

In this Section we focus on the element ratios of various chemical species, and the variations originated in simulations considering a single or multiple explosion events per SNII. In all cases, we analyse the distributions after 1 Gyr of evolution; as we have shown above, at this time differences in simulations SE64 and ME64 have already appeared but the variations in SFRs and total stellar masses are still moderate, allowing to better isolate the effects of assuming single or multiple explosion events per SN from the feedback effects that follow variations in the SFRs. Furthermore, this choice will allow a simpler comparison with the results of our cosmological simulations of the next Section.

We first focus on neutron-capture elements, and show in Fig. 4 the distributions of stellar $[\text{Ba}/\text{Fe}]$, $[\text{Sr}/\text{Fe}]$ and $[\text{Eu}/\text{Fe}]$ as a function of $[\text{Fe}/\text{H}]$ in simulations SE64 and ME64, after 1 Gyr of evolution. We also show the corresponding median values (thick lines) and the $\pm\sigma$ levels (thin lines), as well as a comparison of the distribution functions in the two runs. Clearly, the implementation of multiple explosion times (ME64) has a strong impact in the predicted abundance ratios, particularly in the case of the metal-poor stars with $[\text{Fe}/\text{H}] \lesssim -1$. For $[\text{Fe}/\text{H}] \gtrsim -1$, the mean abundance ratios of stars in the two runs is similar, although the scatter in ME64 is higher. For metal-poor stars the differences between SE64 and ME64 are dramatic, not only in terms of mean/median values, but more importantly in terms of scatter. If a single explosion event per SNII is assumed, as in SE64, the abundance ratios are limited to a narrow range determined by the IMF weighted mean of the stellar yields. In this simulation, the spread in the abundance ratios of Ba, Eu and Sr to Fe is of the order of 0.3 at the most, for all metallicities. In contrast, the abundance ratio of stars in ME64 show not only a much larger scatter up to 2 dex, but also a clear relation between the scatter and the metallicity, such that the scatter decreases with increasing metallicity (a behaviour that extends towards stars with higher abundances). Stars in ME64 have a large variety of possible element ratios, even for coeval stellar populations, which results from the dependence of the chemical yields primarily on the stellar mass, but also on metallicity.

An important observation from the right-hand panels of this figure is that the lowest and highest abundance ratios that are found in ME64, for all three elements, can not be described in SE64; in fact, in ME64 a significant fraction of the stars is in the range of abundance ratios that are absent in SE64. It is also worth mentioning that the abundance ratios $[\text{Ba}/\text{Fe}]$ and $[\text{Sr}/\text{Fe}]$ for the most-metal rich stars are around the solar level, unlike $[\text{Eu}/\text{Fe}]$ which, even for the highest metallicities, presents supra-solar values. This is because, in these simulations, we have ignored the contribution of metals from SNIa and low-mass stars. Eu is not produced by neither of these channels, while Fe is mainly produced by

SNIa. As a consequence, the $[\text{Eu}/\text{Fe}]$ ratio stays high, simply because most of the Fe contribution is missing. In the case of Ba and Sr, however, production by AGB stars counterbalances that of SNIa and, as they are both missing in our models, the ratios stay at solar levels. The results shown here for the very old stars, which is the focus of the present study, are only marginally affected by the contribution of AGB stars or SNIa, as will be discussed in following papers.

Now we turn our focus to the α -elements O, Mg and Si, whose distribution functions and distributions as a function of iron abundance are shown in Fig. 5. In general terms, the behaviour of these elements is similar to that observed for the neutron-captures elements, in the sense that simulation ME64 allows the abundance ratios to vary more compared to SE64, producing more realistic abundance patterns. Furthermore, we can see, in ME64, a positive and strong correlation between $[\text{O}/\text{Fe}]$, $[\text{Mg}/\text{Fe}]$ and $[\text{Si}/\text{Fe}]$ and $[\text{Fe}/\text{H}]$, which is, particularly for very metal-poor stars, opposite to that found in SE64. Similarly to our findings for the neutron-capture elements, for the α -elements we find that in ME64 the spread in abundance ratios decreases with increasing metallicity. It is important to note that, in our simulation ME64, the abundance ratios of neutron-capture elements extend over 3 dex while they spread over 1 dex for the α -elements (although it is higher in the case of oxygen). A similar consideration to our findings for neutron-capture elements, in relation to the $[\text{O}/\text{Fe}]$, $[\text{Mg}/\text{Fe}]$ and $[\text{Si}/\text{Fe}]$ values at solar metallicity, is valid here, as these elements are not entirely produced in SNII events, but also in SNIa which are ignored in these tests.

The results of this Section demonstrate that a correct description of the different ejection-times of release of chemical elements of different mass stars contributing as core-collapse SNe is important in order to properly describe the abundance ratios of various chemical elements, in particular in the case of metal-poor stars and their scatter. We have shown that our model is able to reproduce different levels of scatter in α and neutron-capture elements, which is encouraging given that a similar behaviour is found observationally. Furthermore, we have shown that also the number of predicted very metal-poor stars in the first 200 Myrs can be affected, as well as the star formation itself, given the impact on the cooling rates. Having seen that the model shows the expected features when multiple explosion times are assumed for SNII, we now turn our attention to a more realistic context, and analyse simulations in a cosmological context.

2.3 Tests II - Cosmological simulations

In this Section we use cosmological initial conditions of the formation of a Milky Way-mass galaxy to further test the implementation of multiple explosion times in a more realistic scenario. In particular, we compare the results of two cosmological simulations, referred to as the SE and ME runs (see Table 1), that are identical except for the assumption of single or multiple explosion events per SN, respectively. All input parameters of the code are the same than those used in the idealized simulations in order to facilitate comparison, and similarly, we ignore the effects of SNIa. Including SNIa will have an effect on the predicted element ratios $[\text{X}/\text{Fe}]$, particularly due to changes in the iron abundances. However,

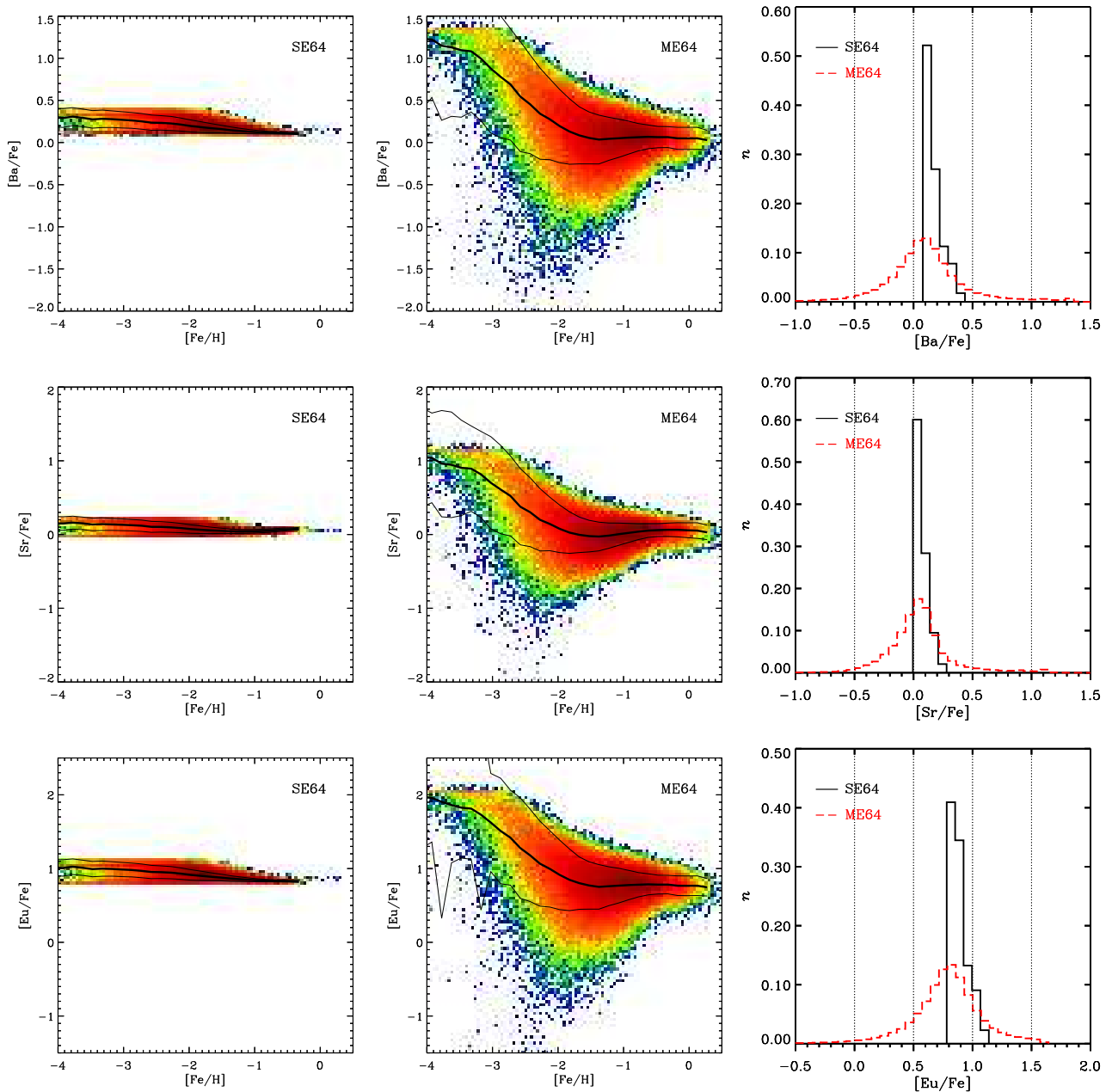


Figure 4. Element ratios of Ba, Sr and Eu in simulations SE64 (left-hand panels) and ME64 (middle-hand panels), after 1 Gyr of evolution. The solid thick and thin lines show, correspondingly, the corresponding median and $1-\sigma$ levels. A comparison of the corresponding element ratio distribution functions in the two simulations are shown in the right-hand panels.

the *shape and features* of the various abundance ratios that are determined by the SNI explosions will not be affected, and therefore are expected to be similar in simulations including SNIa.

2.3.1 Initial Conditions

For the simulations of this Section, we use the cosmological initial conditions of halo named Aq-C of the Aquarius Project (Springel et al. 2008). These correspond to a halo that has, at $z=0$, a mass similar to the Milky Way ($1.6 \times 10^{12} M_{\odot}$), a virial radius of 170 kpc and that is mildly isolated

(no neighbour exceeding half its mass within a sphere of 2 Mpc radius). The simulations start at $z=127$ and run until the present time, i.e. $z=0$.

The ICs are consistent with a Λ -Cold Dark Matter universe with the following cosmological parameters: $\Omega_m = 0.25$, $\Omega_{\Lambda} = 0.75$, $\Omega_b = 0.04$, $\sigma_8 = 0.9$ and $H_0 = 100h \text{ km s}^{-1} \text{ Mpc}^{-1}$, with $h = 0.73$. The mass resolution is $4.1 \times 10^5 M_{\odot}$ and $2.2 \times 10^6 M_{\odot}$ for gas and dark matter particles, respectively, and we have adopted a gravitational softening of 700 pc, fixed in comoving coordinates.

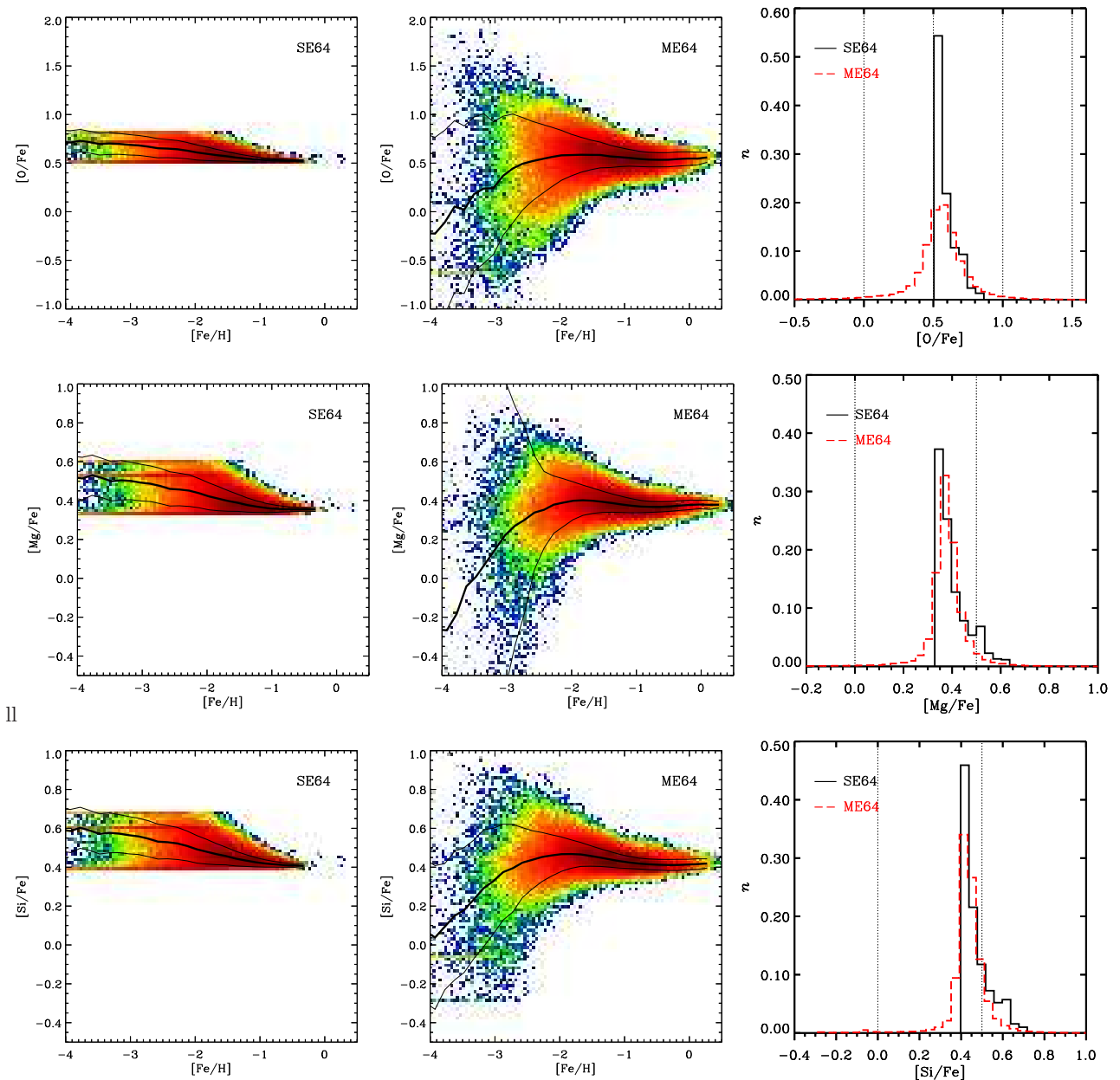


Figure 5. Element ratios of various α -elements, as a function of iron abundance, in simulations SE64 (left-hand panels) and ME64 (middle-hand panels), after 1 Gyr of evolution. The solid thick and thin lines show, correspondingly, the corresponding median and $1-\sigma$ levels. A comparison of the corresponding element ratio distribution functions in the two simulations are shown in the right-hand panels.

2.3.2 Star formation and chemical evolution

In this Section we compare the results of simulations SE and ME, that assume one or multiple explosion events per SNII, respectively, in terms of the SFRs and global chemical properties. As in the case of the idealized simulations of the previous Section, we expect variations in the chemical abundances of the galaxies but also in the SFRs and feedback levels. Furthermore, as our cosmological simulations run up to $z=0$, the cumulative changes during the ~ 14 Gyr of evolution could be much larger than those found for the idealized simulations.

In Fig. 6 we show the SFR and integrated stellar mass

for the simulated galaxies in SE and ME. The SFR in ME is higher to that in SE during the first Gyr of evolution, due to the faster enrichment of the ISM when multiple events per SNII are assumed and the enhanced cooling rates. Later on, however, the behaviour of the SFRs inverts, as the amount of feedback in ME is larger than in SE, producing a stronger reduction of the star formation activity after the first starburst. At the end of the simulation, the galaxy formed in ME has lower stellar mass, but more important is that the growth of the stellar mass in the two simulations has been different, which can induce differences in other galaxy properties such as the final morphology.

In fact, we detect some small differences in the final

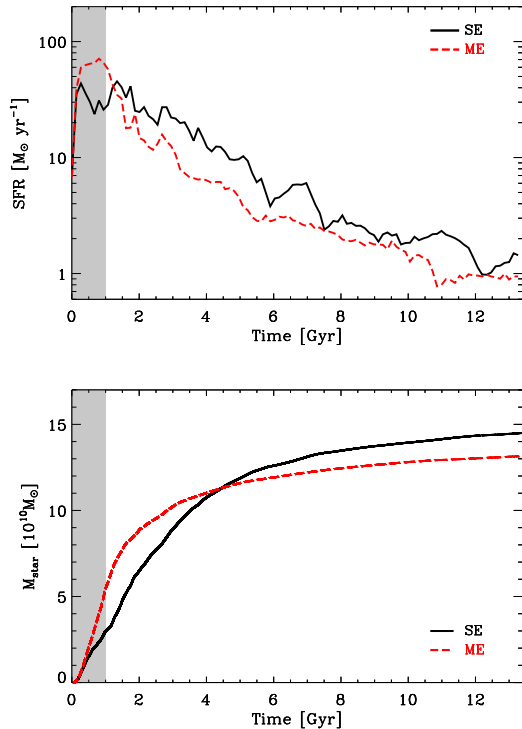


Figure 6. Evolution of the star formation rate (upper panel) and integrated stellar mass (lower panel) for our cosmological simulations SE and ME, which assume single and multiple events per SN explosion, respectively. The shaded area highlights the first 1Gyr of evolution, where we focus our study.

stellar distribution of the simulated galaxies, as can be observed from the face-on and edge-on maps of projected stellar density shown in the left-hand panels of Fig. 7⁷. Although the two galaxies look similar, being composed of a compact, dispersion-dominated bulge and a rotationally-supported disk, the stellar mass is more extended in ME compared to SE, even though the latter has a larger final stellar mass. The rotation of the disks is clearly seen, particularly in the face-on views, from the velocity fields included in this figure. The galaxies also have an extended stellar halo component, which is significantly fainter than the disks and bulges, which we study separately in Section 3. We also find small differences in the final stellar metallicity distributions of the two galaxies, as shown in the right-hand panels of Fig. 7, which are related to the differences in the SFRs and in the stellar distribution. Note however that the variations between the two runs are small, both for the stellar mass density and stellar metallicity, as indicated by the corresponding (logarithmic) color scales.

It is worth noting that the results of our cosmological simulations, during the first 1-2 Gyrs of evolution, are similar to those obtained in the idealized runs of Section 2.2. These early times are of prime importance for the chemical properties of the stars formed in this period. As the chemical abundance of a star is a permanent feature, the old stellar

populations of present-day galaxies will still keep information on the early evolution phases, potentially allowing to reconstruct their star formation and chemical enrichment histories.

2.3.3 Abundance ratios

In this Section we study the abundance ratios of the galaxies formed in our cosmological simulations, and compare results to those of the idealized runs of Section 2.2. Fig. 8 shows the abundance ratios of neutron-capture elements (upper panels) and α -elements (lower panels) as a function of $[\text{Fe}/\text{H}]$ for the galaxy formed in our simulation ME at $z=0$ ⁸. The resulting distributions look similar in broad terms to those found in the idealized simulation (ME64, Figs. 5 and 4); however, some differences appear both in the mean abundance ratios and in the corresponding scatter. These are the result of various effects which are not captured in the idealized simulations, such as gas accretion – which brings unpolluted gas to the systems – and the occurrence of mergers – which contribute ex-situ stars and gas with distinct chemical patterns. In particular, these effects have an impact on the scatter of the low metallicity tail of the distribution. The abundances of the most metal rich stars is also different in the cosmological and isolated simulations, as the former have run for a much longer time. The most important difference between runs ME (cosmological) and ME64 (isolated) runs appears in the $[\text{Ba}/\text{Fe}]$ vs $[\text{Fe}/\text{H}]$ plane. In ME, we detect a group of low-metallicity stars (i.e. $[\text{Fe}/\text{H}] \lesssim -2$) with $[\text{Ba}/\text{Fe}] \lesssim -1$; this region is almost empty in ME64 (Fig. 4), showing the importance of the cosmological evolution in the resulting abundance patterns.

In order to better quantify the effects of considering multiple explosion times per SN event in a cosmological context, we compare in Fig. 9 the distributions of the various element ratios in runs SE and ME, at $z=0$. Given that we are mainly interested in the early chemical enrichment phase which affects more importantly the metal-poor stars, we show results for all stars in the galaxies and also for stars in various $[\text{Fe}/\text{H}]$ bins in order to highlight differences. There are a number of important results revealed by this figure. First, the ME run is able to produce much broader element ratio distributions compared to SE, which, even though in a cosmological context, is unable to produce a broad distribution due to the assumption of a single explosion time for the whole SNI progenitor stars within a star particle. Secondly, we can see that the differences are much more significant for the low abundance ratio tails, for all chemical species considered, and for the lowest $[\text{Fe}/\text{H}]$ bins. Finally, the typical scatter in abundance ratios, particularly for the metal-poor stars, is much larger in the case of the neutron-capture elements than for α -elements (note the different x-ranges plotted).

Having seen that the differential ejection of chemical elements is key to the chemical properties of the very old stars, in the following Section we focus on the stellar halo of the galaxy formed in simulation ME.

⁷ In order to make the projections, we have aligned the total angular momentum of the stars with the z direction.

⁸ The results for SE are very similar to those found for the idealized simulations, in that they show a limited range of possible abundance ratios.

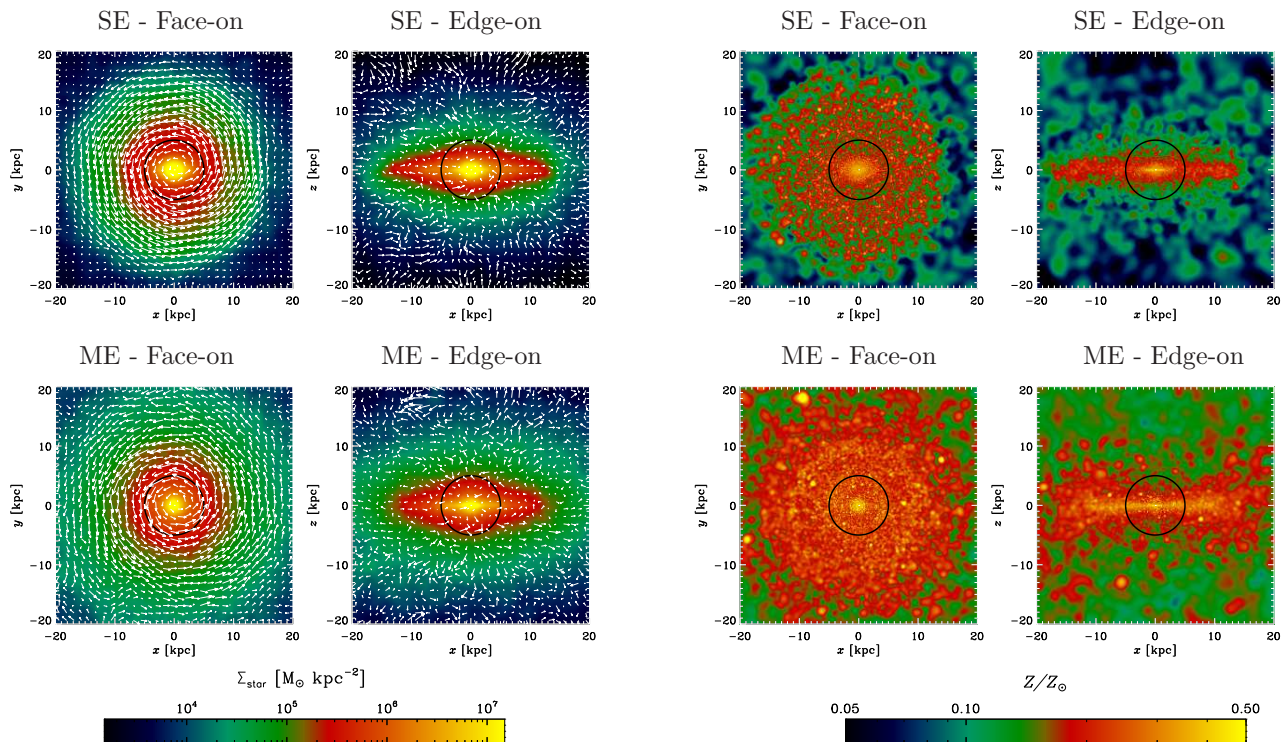


Figure 7. Maps of projected stellar mass density (left-hand panels) and stellar metallicity (right-hand panels) for the simulated galaxies in our cosmological simulations SE (upper panels) and ME (lower panels), at $z=0$, in face-on (xy) and edge-on (xz) views. The white arrows in the mass density maps indicate the corresponding velocity fields and reveal that, at the present time, the simulated galaxies have an extended, rotationally-supported disk-like component and a compact bulge.

3 ABUNDANCES IN THE STELLAR HALO

In the previous Section we have shown that the implementation of multiple explosion times per SNI event has a significant impact on the chemical properties of stars, particularly those formed during the early enrichment phases. We have demonstrated that the properties of the ISM at early times leave chemical imprints in the old stellar populations of present-day galaxies, such as the stellar halo and the old bulge components. In this Section we study the chemical properties of the stellar halo formed in our cosmological simulation ME, focusing on the abundance ratios of various chemical elements and their scatter. In a second paper of this series, we discuss results for the old bulge component.

In order to study the stellar halo, we first need to determine how we define the halo stars as, in the simulations, there are many different ways to assign stars to this (or any other) component. In this work, we define the stellar halo using stars that formed during the first Gyr of evolution and that are, at the present day, outside a sphere of 5 kpc from the center of the galaxy⁹. Our choice, based only on the age

and present-day radius of stars, provides us with a simple, easy to interpret and clean sample, without the need to make any additional assumption on the properties of the halo (e.g. metal content or dynamics)¹⁰. Furthermore, the use of stars outside the very central region provides a sample that is uncontaminated by the old bulge population¹¹.

The left-hand panels of Fig. 10 show maps of the present-day spatial distribution of the old stars (i.e. formed in the first Gyr) in our simulation ME, up to 20 kpc (i.e. the inner halo) and to 1/4 of the virial radius (i.e. the extended halo). Also indicated is the minimum radius assumed for halo stars, i.e. 5 kpc. The figure shows two different projections, in order to highlight the morphology of the stellar halo, which correspond to the face-on and edge-on views of Fig. 7. Note that, unlike the whole stellar population, the old halo stars define no preferred plane, although the stellar distribution is not fully spherical. The simulated stellar halo is spatially extended, has low surface mass density, and exhibits, particularly in the outermost regions, substructure

⁹ The choice of 1 Gyr is somewhat arbitrary. However, we note that our results are not very sensitive to this selection, except when we go to the very old populations, as we discuss in Appendix B. Also, note that we select stellar halo particles at $z=0$, as this simplifies the interpretation of results and the comparison with observational data.

¹⁰ Note that our sample could include thick disk stars, if this component was formed in the first Gyr of evolution. We have verified, however, that the majority of the simulated stellar halo does not have a significant degree of rotation.

¹¹ We have tried several threshold radii to define the halo and found that our results are not sensitive to this choice, provided $r \gtrsim 4$ kpc.

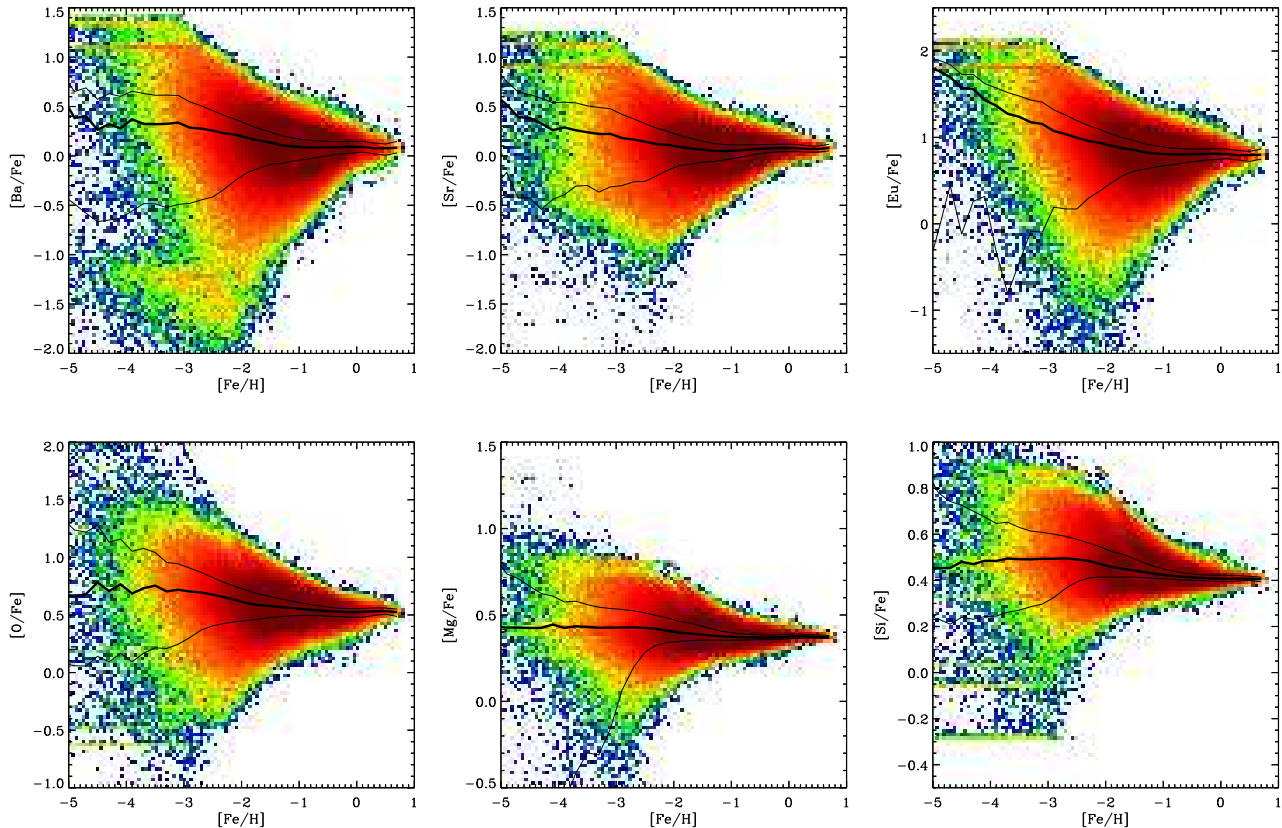


Figure 8. Element ratios of neutron-capture and α -elements as a function of the iron abundance, at $z = 0$, for the galaxy formed in our cosmological simulation ME.

in the form of stellar clumps. A stellar stream, reminiscent of observed streams, is also detected in the face-on view.

3.1 Metallicity distribution

The right-hand panels of Fig. 10 show maps of the stellar metallicity of the old stars (formed in the first Gyr) in simulation ME, for the same views and spatial scales shown in the left-hand panels of this figure. While the inner halo ($5 \leq r < 20$ kpc) is characterized by average stellar metallicities of the order of $Z/Z_{\odot} \sim 0.1$ or higher, stars that are further away (i.e. in the outer halo) are less enriched, with typical (spatially-averaged) metallicities between $Z/Z_{\odot} \sim 0.05$ and $Z/Z_{\odot} \sim 0.1$. The stellar stream is more metal-rich compared to the rest of the outer halo population, suggesting that these stars were formed in an accreted satellite and were not formed *in-situ*.

Fig. 11 shows that there is, in fact, a metallicity profile in the halo. In this figure we show the mean metallicity of the halo stars as a function of radius, averaged over 2 kpc-wide radial bins. For reference, we also show the corresponding surface stellar mass density profile (dashed-dotted line). We find that the simulated stellar halo exhibits a metallicity profile for $r \lesssim 50$ kpc, where most of the stellar halo mass is concentrated. Note that the surface mass density declines

rapidly, changing by approximately 3 orders of magnitude between 5 kpc and the virial radius¹².

3.2 Abundance ratios

We analyse in this Section the abundance ratios and scatter of the different elements in the simulated stellar halo in our run ME, and compare them to observational results. Fig. 12 shows the distributions of α - and n -capture elements, relative to Fe, as a function of the $[\text{Fe}/\text{H}]$ abundance. The black thick and thin lines indicate respectively the median and $1\text{-}\sigma$ levels. We also include the observational results of Roederer et al. (2014) and Yong et al. (2013) (only carbon-normal stars), which provide data on the abundances of metal-poor stars in our Galaxy. We note that the samples are expected to be complete only for the low metallicity range, approximately at $[\text{Fe}/\text{H}]$ abundances lower than -2.5 or -3 .

The abundance ratios of stars in the simulated halo are similar to those obtained for the whole stellar population (Fig. 8), with the expected differences in the $[\text{Fe}/\text{H}]$ levels. In particular, the α -elements have lower scatter lev-

¹² Note that all bins with $r \lesssim 170$ kpc contain more than 100 star particles, and all bins with $r < 125$ kpc have at least 10000 star particles. In the figure, the black dotted line denotes the 100 stellar particle threshold.

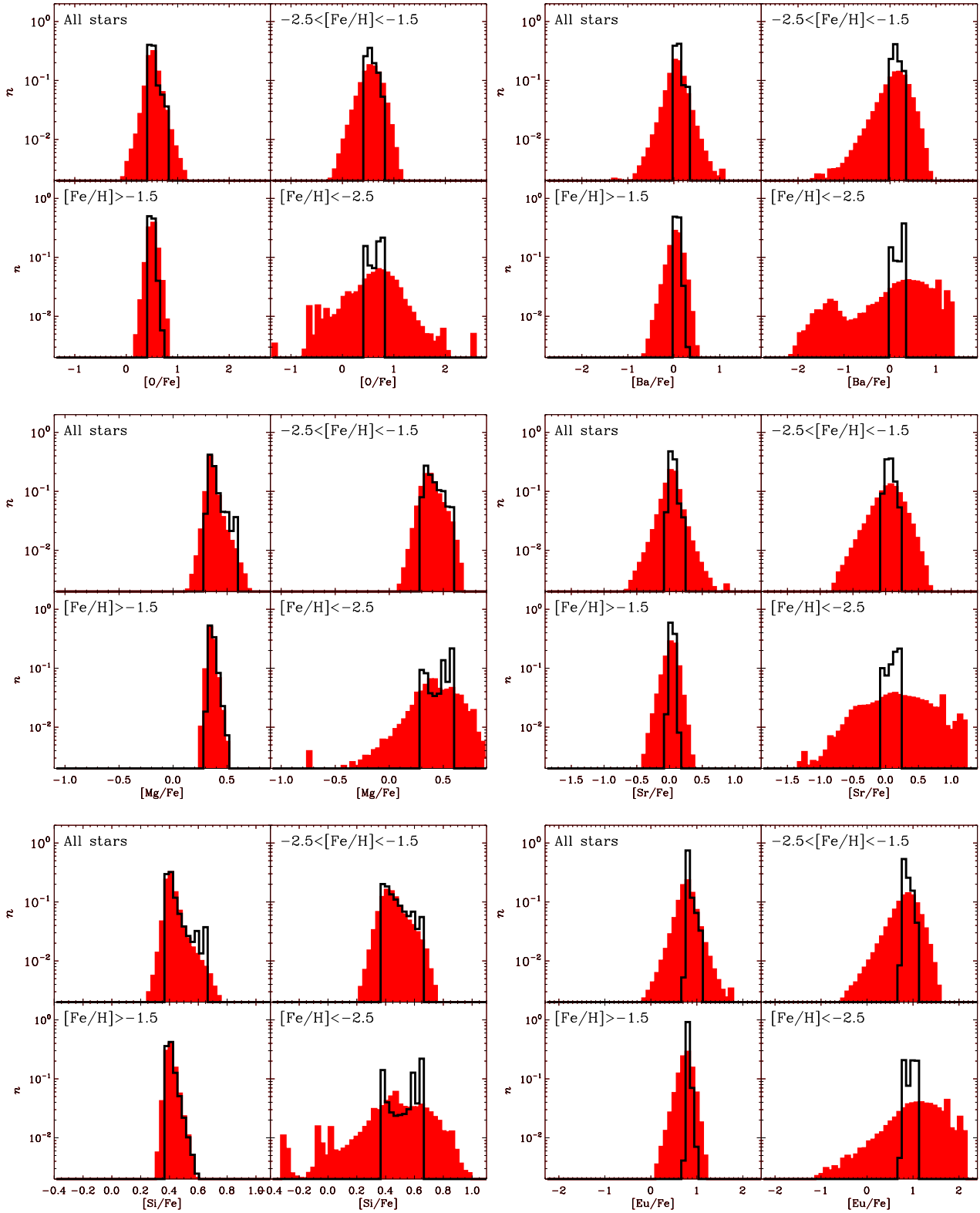


Figure 9. Distribution functions of various stellar abundance ratios, for our cosmological simulations SE (solid lines) and ME (shaded areas), at $z = 0$. The different panels show distributions for four ranges in $[\text{Fe}/\text{H}]$.

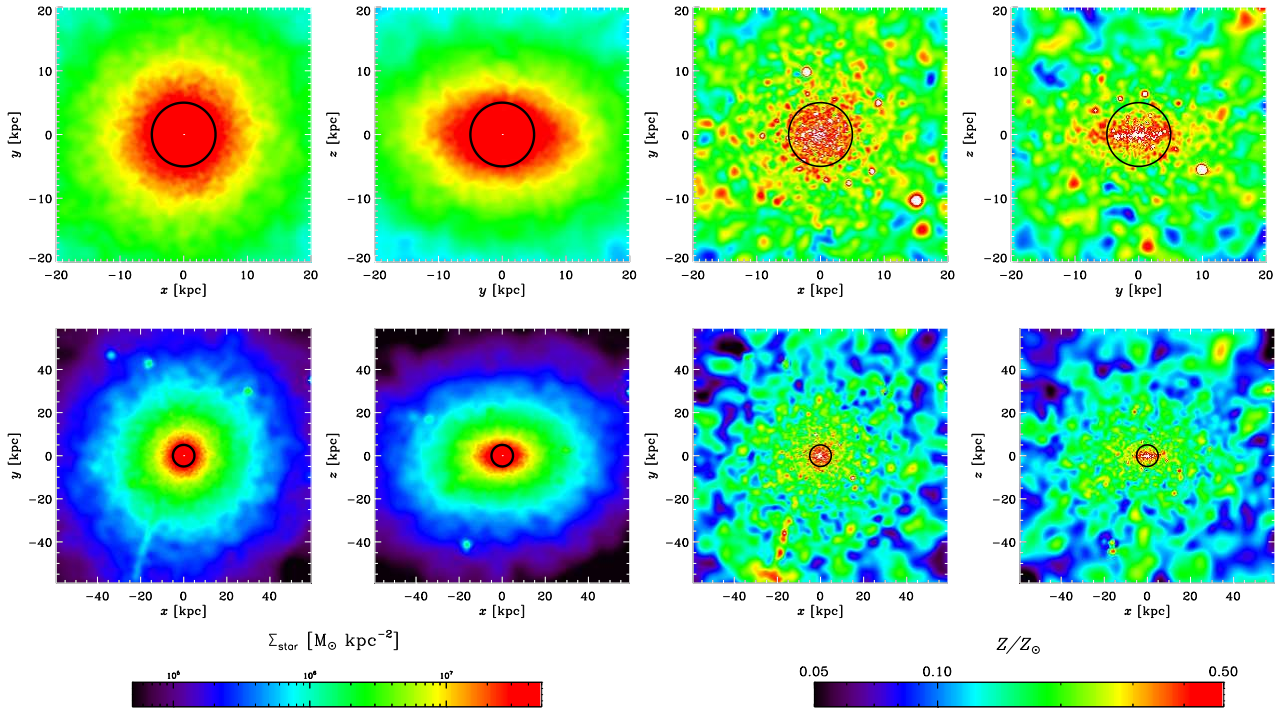


Figure 10. Maps of projected stellar mass density (left-hand panels) and stellar metallicity (right-hand panels), at $z=0$, for our cosmological simulation ME, considering stars that formed in the first Gyr of evolution. In both cases we show two perpendicular projections, corresponding to the face-on and edge-on projections of Fig. 7. The black circle shows our threshold of 5 kpc to define halo stars. The upper- and lower panels show, respectively, the inner galaxy and a zoom-out up to 0.25 of the virial radius. Note that the color code and scale have been chosen in order to highlight the halo density and metallicity structure (note that these are different from those used in Fig. 7).

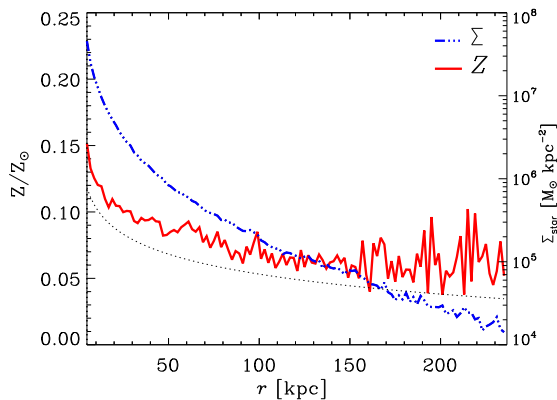


Figure 11. Stellar surface mass density (Σ_{star} , dashed-dotted line) and mean stellar metallicity (Z , in solar units, solid line), as a function of radius, of the halo stars (formed in the first Gyr and, at $z=0$, outside the inner 5 kpc) in the galaxy formed in our cosmological simulation ME. Each bin covers 2 kpc in radius, and the black dotted line indicates the limit of 100 particles per bin.

els compared to the n -capture elements¹³. In general, we

¹³ It is worth noting that a small but non-negligible fraction of

find a good agreement with the observational data, particularly in the low metallicity region where the samples are approximately complete. The most important disagreement occurs for $[\text{Eu}/\text{Fe}]$ and $[\text{Ba}/\text{Fe}]$, where the simulation predicts higher abundances compared to the observational results.

In order to better quantify the agreement between the simulation and the observational data, Fig. 13 shows the mean, median, and $1-\sigma$ values of the distributions of the various elements, as a function of the $[\text{Fe}/\text{H}]$ ratio. The bins are 0.5 dex wide, such that each bin has at least 5 data points in the observational samples. As seen in the previous figure, we find in general a very good agreement between the simulation and the data for the α -elements Si and Mg. In particular, the abundances of these elements agree very well with the Roederer data while the Yong data lies below. We find excellent agreement between the simulation and the data for the scatter of these elements, except for the low metallicity bins in the distribution of $[\text{Mg}/\text{Fe}]$. In the case of $[\text{O}/\text{Fe}]$, the scatter levels of the simulation are consistent with the observations for $[\text{Fe}/\text{H}] \gtrsim -3$, while the mean and median values are systematically lower compared to the data.

stars have $[\text{Ba}/\text{Fe}]$ ratios $\lesssim -1$, different from the overall distribution which has higher $[\text{Ba}/\text{Fe}]$ values. We come back to the origin of this group in Section 3.3.3.

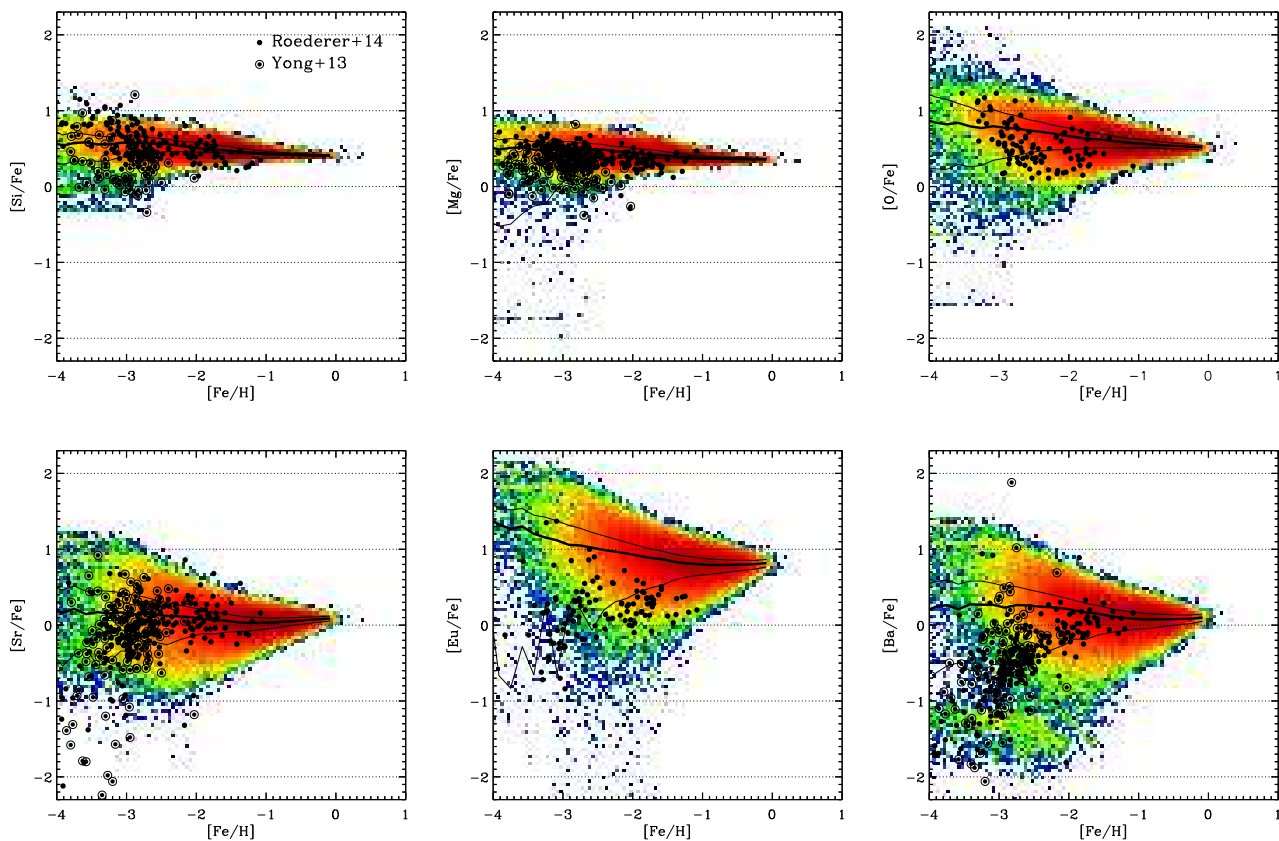


Figure 12. The various abundance ratios as a function of $[\text{Fe}/\text{H}]$ for the halo stars in our simulation ME. The solid thick and thin lines show, correspondingly, the corresponding median and $1-\sigma$ levels. We also include the available observational data of Roederer et al. (2014, solid circles) and Yong et al. (2013, encircled symbols) for metal-poor stars in the Galaxy.

We now turn our attention to the neutron-capture elements. In this case, we find an excellent agreement between the two observational data sets and the simulation for $[\text{Sr}/\text{Fe}]$, with very similar scatter levels for all metallicity bins. We also detect a good agreement for $[\text{Ba}/\text{Fe}]$ for the bins corresponding to $[\text{Fe}/\text{H}] \gtrsim -2.5$, although the simulation predicts higher mean, median and scatter values for the lower metallicity bins. As already seen in the previous figure, the $[\text{Eu}/\text{Fe}]$ values and scatter are systematically higher in the simulation compared to the data, for all metallicities.

The disagreement of the predicted $[\text{Eu}/\text{Fe}]$ with the observational data is expected; Eu is produced only at short time-scales, typical of the massive stars, while iron has an important contribution of SNIa and low mass stars, which enrich the ISM in longer time-scales. In this simulation, we only considered enrichment by massive stars, and so our simulation does not produce the typical “knee” (decreasing trend of $[\text{Eu}/\text{Fe}]$) that would appear if the enrichment at longer time-scales is included. On the other hand, the simulation does reproduce the trend for $[\text{Ba}/\text{Fe}]$ and $[\text{Sr}/\text{Fe}]$, as Ba and Sr are also produced in SNIa and AGB events in longer time-scales. For these elements, the missing contribution of SNIa/AGB to Ba and Sr in the simulation is approximately counterbalanced by the missing contribution of Fe via SNIa, producing trends similar to those observed. Finally, we note that the agreement between the simulation and the data is

better for Sr than for Ba, even though these elements are produced in the same events. The reason for this is likely that there is smaller difference between the production of Sr by massive stars and r-process, compared to that of Ba.

It is worth noting that our results on the distribution functions of our halo stars sample might be affected by the selection of our halo stars sample, particularly the age threshold considered. We performed several tests varying this parameter and found that our results are not strongly affected by this choice, although some differences are still visible, as we discuss in Appendix B.

3.3 The $[\text{Sr}/\text{Ba}]$ ratio

In this Section we discuss the predictions of our model for the $[\text{Sr}/\text{Ba}]$ ratio, and compare them with observational data and with the predictions of stochastic chemical abundance models. The $[\text{Sr}/\text{Ba}]$ ratio is important as it is sensitive to the origin of the heavy elements. Observationally, not only the $[\text{Sr}/\text{Fe}]$ and $[\text{Ba}/\text{Fe}]$ show a dispersion in our Galactic halo, but also their ratio $[\text{Sr}/\text{Ba}]$ is not constant (François et al. 2007). These observations confirm the need for a second neutron-capture process which synthesised differently the light elements (such as Sr) and the heavy ones (as Ba), in addition to the r-process. Early contribution from fast ro-

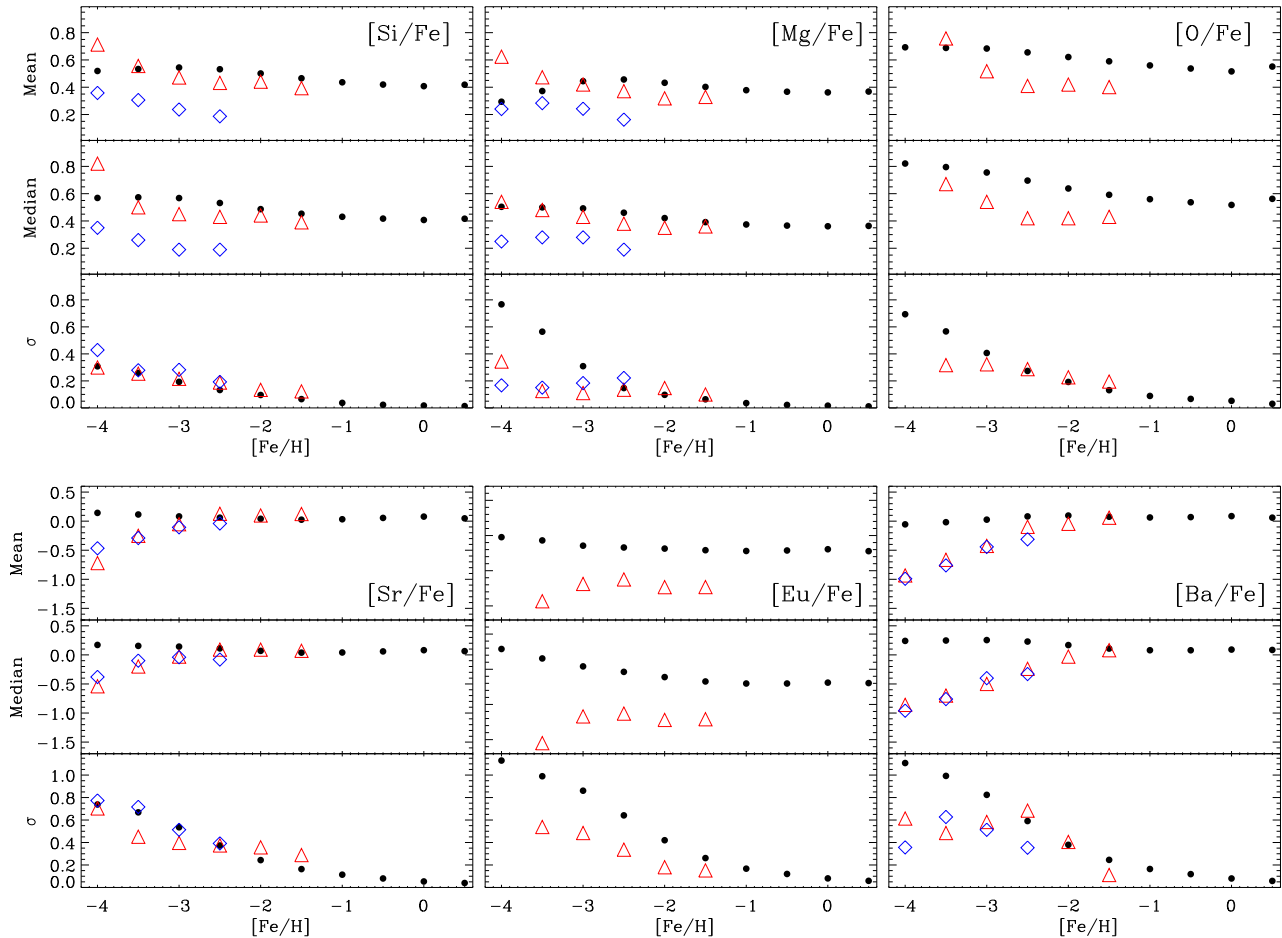


Figure 13. Mean, median and $1-\sigma$ values for the different elements in our halo stars in simulation ME (black). The open symbols correspond to the observational data from Roederer et al. 2014 (red triangles) and Yong et al. 2013 (blue diamonds).

tating massive stars to s-process elements has been proposed (Pignatari et al. 2008; Chiappini et al. 2011; Frischknecht et al. 2012; Chiappini 2013), as normal s-process enrichment by AGBs operates on long time-scales (> 300 Myr, see Cescutti et al. 2006); moreover, at low metallicity it is expected from AGB nucleosynthesis a $[\text{Sr}/\text{Ba}] < 0$ (Cristallo et al. 2009, see also Frebel 2018).

These ideas were recently incorporated in stochastic inhomogeneous chemical evolution models which were able to predict a scatter in the $[\text{Sr}/\text{Ba}]$ ratio (Cescutti et al. 2013; Cescutti & Chiappini 2014). These models however, not being in the cosmological framework, do not take into account additional scatter caused by the addition of ex-situ stars resulting from mergers. These smaller galaxies would have their own star formation histories which, in principle, could add more scatter into the more simplified picture of the stochastic inhomogeneous chemical evolution models. In the following sections we compare the predictions of our simulations in a cosmological context to those obtained with these previous models.

3.3.1 $[\text{Sr}/\text{Ba}]$ scatter in our cosmological simulations compared with observations

Figure 14 shows the $[\text{Sr}/\text{Ba}]$ abundance ratio of the simulated halo stars at $z=0$ as a function of $[\text{Ba}/\text{H}]$ (left-hand panel) and $[\text{Fe}/\text{H}]$ (middle-hand panel), together with the two observational data sets used in this work¹⁴. The $[\text{Sr}/\text{Ba}]$ vs $[\text{Ba}/\text{H}]$ relation is a better way to compare simulations and observations because, as explained before, we are ignoring enrichment via SNIa which affects the iron abundance, but not the $[\text{Sr}/\text{Ba}]$ ratio. The simulated stellar halo is characterized by sub-solar $[\text{Sr}/\text{Ba}]$ values, although a fraction of the stars have $[\text{Sr}/\text{Ba}] > 0$ depending on the metallicity. From this figure we can also observe a group of stars with $[\text{Sr}/\text{Ba}] \sim 0.8$, whose origin we discuss below.

The simulation is able to reproduce both the high and low $[\text{Sr}/\text{Ba}]$ values observed in the Galactic halo, due to the combined pollution of r - and s -process elements in fast rotating massive stars, our implementation of the differential

¹⁴ We note that, for the sake of clarity, we have not included the observational errors in the figure, although these are usually of the order of 0.2-0.3 dex for $[\text{Sr}/\text{Ba}]$ and 0.1 dex for iron.

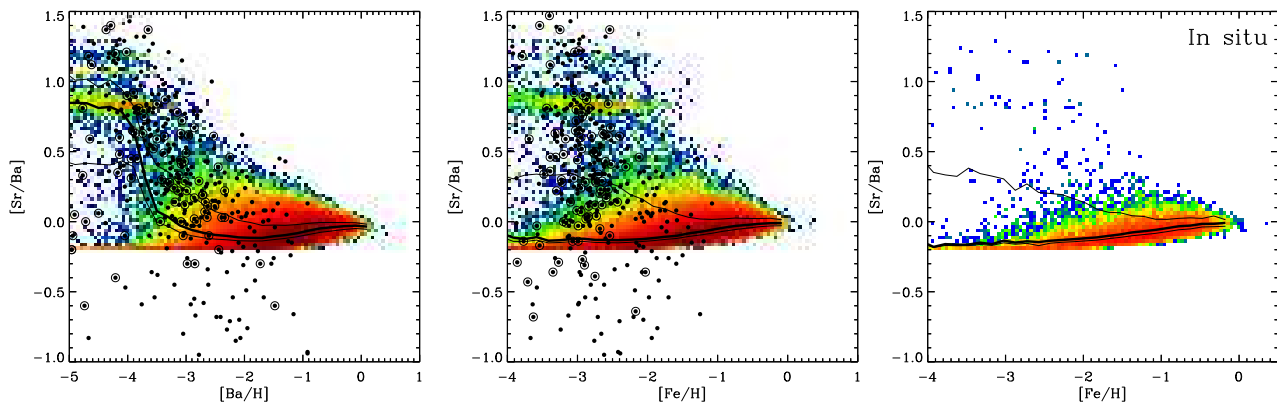


Figure 14. $[\text{Sr}/\text{Ba}]$ abundance as a function of $[\text{Ba}/\text{H}]$ (left-hand panel) and $[\text{Fe}/\text{H}]$ (middle-hand panel) for the simulated halo stars, together with the observational data of Roederer et al. (2014) and Yong et al. (2013). The right-hand panel of this figure shows the $[\text{Sr}/\text{Ba}]$ vs $[\text{Fe}/\text{H}]$ relation for the simulation, only considering the in-situ stars. The solid thick and thin lines show, correspondingly, the corresponding median and $1-\sigma$ levels.

enrichment of stars with different masses, and the cosmological evolution. However, in the simulation there are no stars with $[\text{Sr}/\text{Ba}] < -0.3$, a limit which is determined by the stellar yields adopted (see Cescutti et al. 2013 for a discussion).

3.3.2 $[\text{Sr}/\text{Ba}]$ scatter: cosmological simulations compared to inhomogeneous chemical evolution models

In Fig. 15 we show the comparison between the results for $[\text{Sr}/\text{Ba}]$ of the Cescutti et al. (2013) model (left-hand panel) and the results of our simulations for ex-situ (middle-hand panel) and in-situ (right-hand panel) halo stars. The results are presented as a function of oxygen instead of iron because the former is a tracer for the star formation history.

Compared to the results of our SPH simulation, the results in Cescutti et al. (2013) cover a narrower range of metallicity. In the metal-rich end, this happens because the stochastic models used the present day halo metallicity distribution, at the solar vicinity, as a constraint. However, we now know that a large portion of the stars between $[\text{Fe}/\text{H}] = -1$ and below are actually part of debris of galaxies accreted onto the Milky Way in the past (Helmi 2020 and references therein). Therefore, one can say that the constraint adopted in Cescutti et al. (2013) is already biased to ex-situ stars. On the other hand, towards the lower metallicities, the low dilution of the contribution of a single SNI by the ISM is a free parameter. Taken into account these differences, the results we obtain for the ex-situ stars seem to match remarkably well the results obtained by the more simplified approach of the stochastic models used in Cescutti et al. (2013).

What is more important in this comparison is to see that in the stochastic model the high- $[\text{Sr}/\text{Ba}]$ population is very old, formed before the r -process events start to enrich the ISM, lowering this ratio. The reason is that in the stochastic volume the mixing is instantaneous and the typically abundant r -process enrichment erases the chemical signature of the rotating massive stars pollution.

The fact that the high- $[\text{Sr}/\text{Ba}]$ stars are very old appears to be also in agreement with our more realistic simulations shown in the present paper. We expect this outcome

to be correct even if we consider a different r -process event, as it is the case for the stochastic approach (as illustrated in Cescutti & Chiappini 2014 for magneto rotational driven SNe and in Cescutti et al. 2015 for neutron star mergers), although the exact definition of the age range expected for these stars can vary depending on the nucleosynthetic assumptions. This stresses the importance to obtain a high-resolution in age estimates in the very early phases of the galaxy assembly. The first steps in this direction were recently shown by Montalbán et al. (2021).

3.3.3 The origin of the high $[\text{Sr}/\text{Ba}]$ stars

The sub-population of stars with low $[\text{Ba}/\text{Fe}]$ values identified in Figure 12 can also be seen in the distribution of $[\text{Sr}/\text{Ba}]$, as a subpopulation with $[\text{Sr}/\text{Ba}] \sim 0.8$ in Figure 14. In order to understand the origin of this group, we first analyze the formation of the halo stars within the cosmological context of our simulation, where galaxies and haloes grow via the continuous aggregation of matter and smaller substructures. In the simulation, we can trace back the formation of the $z=0$ system identifying, at each time, the main progenitor – i.e. the most massive structure at that time – and a series of smaller systems and material that later accreted onto the main progenitor.

Figure 16 shows a series of snapshots of the distribution of all stars that ended up in the main progenitor at $z=0$ (upper panels), and in the stellar halo component (lower panels). We focus on the early evolution, and show the distributions at 1, 2, 3 and 4 Gyr, characteristic of the formation and accretion of today’s halo stars. The figures are centered at the mass center of the main progenitor at the different times, and the circles indicate the position and size of the different subhalos of the simulation, including the main progenitor. The upper panels of this figure reveal that, as expected within the cosmological context considered, the stellar component of the simulated galaxy has a contribution of material formed in systems other than the main progenitor. If we consider all stars that form the $z=0$ progenitor (i.e.

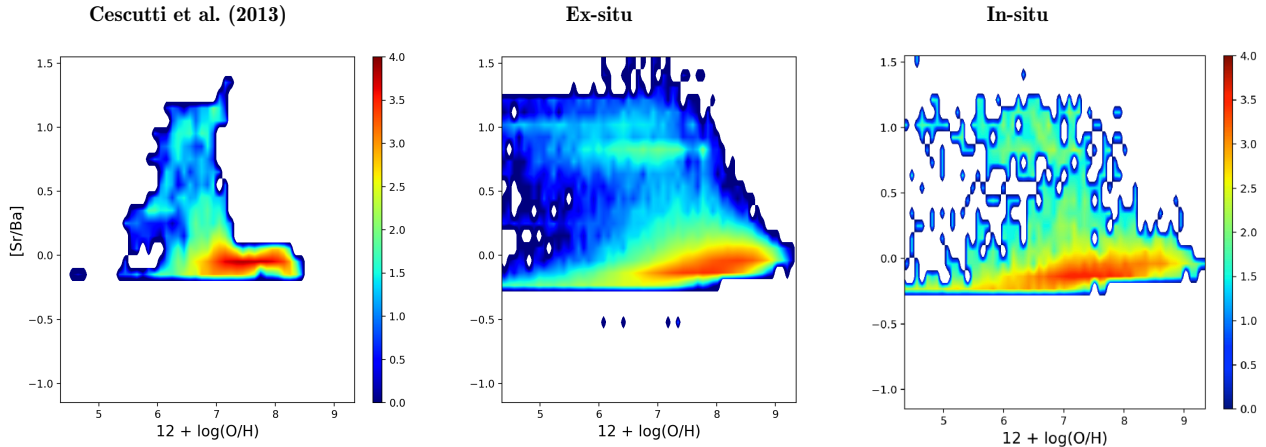


Figure 15. Distribution of $[\text{Sr}/\text{Ba}]$ as a function of oxygen abundance for the halo stars in the Cescutti et al. 2013 model (left-hand panel), and the ex-situ (middle-hand panel) and in-situ (right-hand panel) components of the stellar halo in our cosmological simulation.

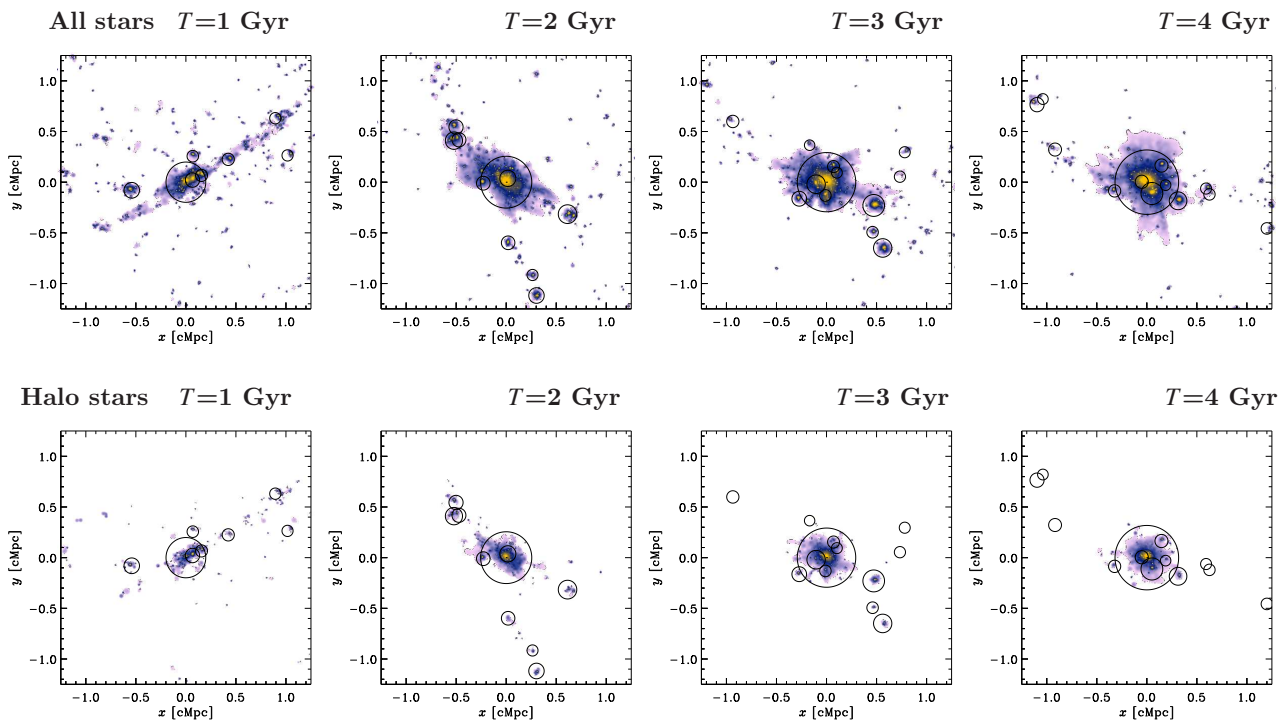


Figure 16. The spatial distribution of stars that ended up in the main galaxy at $z = 0$, after 1, 2, 3 and 4 Gyr of evolution. The upper panels include the whole stellar population, while the lower panels are restricted to stars that ended up in the stellar halo component. The black circles show the position of the main progenitor and the most massive satellite galaxies at the various times; their sizes are scaled with the corresponding masses. The colour scale represents the density of stellar mass in logarithmic scale, to allow a better visualization of the halo stars and their spatial location.

all stellar components), the fraction of stellar mass that has been accreted is small.

However, the simulated stellar halo has significant contribution of stars formed in small satellite systems that were later accreted onto the main progenitor – the so-called *ex-situ* stars. The ex-situ fraction of our simulated halo is 0.8, i.e., only 20% of the stars in today’s halo formed in the main progenitor. This means that most halo stars formed in smaller, more metal-poor systems, with more episodic star

formation activity, compared to the main progenitor. A high ex-situ fraction of the stellar halo is consistent with observations of the Milky Way stellar halo, although in our simulation many small satellites contributed to the stellar halo, while recent discoveries suggest that a large part of the Milky Way’s stellar halo could be the result of an early and massive accretion event (Helmi et al. 2018; Belokurov et al. 2019 – see review by Helmi 2020 and references therein).

It is worth noting that the ex-situ stars that end up

in the stellar halo locate preferentially in the outskirts of their systems before accretion. The reason for this behaviour is that stars in the outer regions are the less bound stars, likely to be lost during the merger. As a result, these stars stay in the halo component and are not able to reach the bulge region, unlike the central, most bound stars. How this compares to the most recent observations of the Milky Way bulge will be addressed in a following paper.

Because of the characteristics of the cosmological evolution, the chemical properties of the halo stars are a result of two effects: the mass of the system where they formed, and their location with respect to its centre before accretion. The properties of halo stars that we see today have therefore encoded information on their formation sites, particularly in terms of r - and s -process products. In this framework, it is possible to understand the origin of the sub-population of stars with low $[\text{Ba}/\text{Fe}]$ and high $[\text{Sr}/\text{Ba}]$. The right-hand panel of Figure 14 shows the $[\text{Sr}/\text{Ba}]$ vs $[\text{Fe}/\text{H}]$ relation for halo stars, restricted to the in-situ component. We can observe that the majority of the stars with high $[\text{Sr}/\text{Ba}]$ are absent, indicating that most of this component is ex-situ¹⁵. Note that the key ingredient for forming the high $[\text{Sr}/\text{Ba}]$ stars is the time-scale, because it is only the very old stars that can be polluted with Sr before the ISM is contaminated with Ba. This is illustrated in Figure 17 (see also Appendix B), where we show the differences in the distributions of $[\text{Sr}/\text{Ba}]$ for stars 1 Gyr (black) and 100 Myr old (red). We find that restricting the halo sample to the oldest stars results in a wider distribution. In particular, we find a significant fraction of $[\text{Sr}/\text{Ba}] \sim 0.8$ stars for $\tau = 100$ Myr, while for our fiducial halo sample the distribution peaks at $[\text{Sr}/\text{Ba}] \sim -0.3$ with a minimum contribution of high $[\text{Sr}/\text{Ba}]$ stars. Therefore the existence of these high $[\text{Sr}/\text{Ba}]$ stars is a result of the enrichment time-scales for rotating massive stars compared to those assumed for the r -process and to the ages of accreted stars. Indeed, this feature is less prominent when plotting in-situ stars in Fig. 14 and this is due to the fact that, as shown before, many of the oldest stars were formed in accreted systems.

4 DISCUSSION AND CONCLUSIONS

In this paper we present a novel implementation of chemical enrichment in hydrodynamical, cosmological simulations, which considers the production of α - and neutron-capture elements, and their distribution into the interstellar medium during SNI_{II} explosions. The novel aspect of our work is twofold: first, we use chemical yields which consider the impact of the rotation of massive stars at low metallicity (Cescutti & Chiappini 2014; Cescutti et al. 2015) and, second, we consider the differential enrichment due to the different life-times of stars of different mass within the massive star range. In other words, we do not use IMF weighted yields for core collapse SNe. This means that the star particles of the simulations, which represent a mix of individual stars with given masses, *explode* in several episodes rather than at a single time, as usually done in this type of numerical studies.

¹⁵ Although there are still some in-situ stars with high $[\text{Sr}/\text{Ba}]$ ratios; this is likely an artifact of the algorithm to identify sub-haloes in the simulation, as it excludes the very small systems.

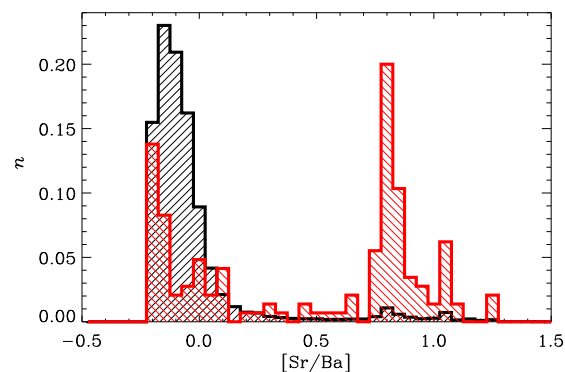


Figure 17. Normalized distribution functions of $[\text{Sr}/\text{Ba}]$ for our fiducial halo sample ($\tau = 1$ Gyr, black) and for the very old stars ($\tau = 100$ Myr, red) in our cosmological simulation ME.

This might produce small variations in the overall chemical properties of galaxies; however, it has a critical role for the oldest/most metal-poor stars which are severely affected by the early enrichment stages, a point which we demonstrated here.

The main aim of the work was to investigate whether our model can reproduce the different scatter levels for the abundance ratios of the α - and neutron-capture elements, as suggested by observations of old stars in our Galaxy. We focused on the abundance ratios and scatter of the α -elements O, Si and Mg, and of the neutron-capture elements Ba, Eu and Sr, relative to the Fe abundance, and compared the predictions of simulations that assumed either one or multiple explosions per star particle – i.e. the “single explosion” (SE) and “multiple explosions” (ME) models. All simulations of this work assumed, for the ME model, a number of 5 explosions per SNI_{II} event, in order to avoid large numerical overcosts.

Our implementation is grafted onto the GADGET3 code (Springel et al. 2008) with the sub-grid modules of Scannapieco et al. (2005, 2006) for cooling, star formation, chemical enrichment and feedback from supernova (type II and Ia) explosions. As the current work focuses on the chemical abundances of the old stellar population, which are mainly determined by the products of SNI_{II} explosions, we have switched off the module for SNIa (as well as the Poulhazan et al. 2018 extensions for AGB stars) in all simulations presented here.

In order to validate and test our implementation, we run a number of idealized simulations of isolated galaxies, as well as the cosmological formation of a Milky Way-mass galaxy, and compared the chemical properties of the resulting systems for the SE and ME models. We found that the chemical abundance ratios obtained for all chemical elements are different for the SE and ME models: while in the former the abundance ratios are restricted to a narrow range given by the yields tables, the latter are able to produce much more diverse abundance ratios, in better agreement with observational results. The ME models produce a faster enrichment of the interstellar medium, because the first *explosion* event associated to star particles occurs earlier compared to the SE models, which affects the cooling, star formation and feedback levels at the very early times. Although the interplay between cooling, enrichment, star formation and feedback is

non trivial, all our ME simulations produced galaxies with a larger final stellar mass compared to the SE runs due to the increased cooling at early times. We have performed simulations at different resolutions and changing the number of neighbours over which we distribute the metals and, in all cases, we found that the abundance ratios and scatter of all elements do not vary significantly, indicating that our results are numerically robust.

After passing the various numerical tests performed to our implementation, we focused on the chemical properties of the *stellar halo* formed in our cosmological simulation ME. In order to define this component, we used star particles that, at $z = 0$, are outside a sphere of 5 kpc from the centre of the galaxy (as to avoid the bulge region which will be discussed in a separate paper) and that formed during the first Gyr of evolution. Our main findings can be summarized as follows:

- The scatter found for the abundance ratios of neutron-capture elements (relative to iron) of the old stars is larger compared to that of α -elements. We find that the α -elements have a typical scatter of the order of $\lesssim 0.5$ dex (even at low metallicity), while for all neutron-capture elements studied here the scatter levels are of the order of 1 dex or higher. For both types of elements, the scatter increases for decreasing metallicity, although this trend is much more pronounced for the neutron-capture elements.

- *The main reasons for the different levels of scatter found for the neutron-capture and α -elements are the dependence of the stellar yields with the properties of the massive stars and the description of the differential enrichment during the early phases.*

- Our model reproduces the abundances and scatter in [Sr/Ba], showing the importance of fast-rotating stars for the old stellar populations. In particular, the model is able to reproduce the formation of high [Sr/Ba] stars. Again, the key factor in producing such high [Sr/Ba] ratios is the enrichment level of the ISM, as such ratios are produced when Sr has already enriched it but Ba has not.

- Our simulation shows that the cosmological setting also contributes to the scatter of the different elements because sub-populations of stars formed in different systems end up in the main progenitor stellar halo at $z = 0$. Our simulated halo has a significant contribution of accreted stars, with an ex-situ fraction of 0.8. This is particularly important for the [Sr/Ba] ratio and the corresponding scatter level: as lower mass systems have a slower ISM enrichment compared to the main progenitor, they contribute stars with large [Sr/Ba] ratios to the $z = 0$ stellar halo of the simulated galaxy.

Observationally, the contribution of satellites to the Milky Way stellar halo could be tested at least in two different ways. First, by measuring the fraction of the stellar population of present dSph with high [Sr/Ba]; in this case, it is also possible to investigate the dependence on the galactic masses, e.g. whether the lightest galaxies are those with the highest values of [Sr/Ba]. The second opportunity would be to check whether stars now in the Galactic halo with a high [Sr/Ba] show different characteristics from those with low or intermediate [Sr/Ba] ratio, which would point to their origin as debris of satellites merged to our halo (e.g. [Helmi et al. 2018](#)). On this subject, [Roederer et al. \(2018\)](#) have found

an indication that r -process rich stars could actually have belonged to small systems.

- Our simulations properly describe the early chemical enrichment by the most massive stars, thanks to the implementation of differential enrichment due to the different mass stars. Such early enrichment of the medium leaves an imprint in the abundances of the very old stars. This opens up the possibility to reconstruct the level of enrichment of the ISM at early epochs from observational data of the old stars in galaxies, information that is otherwise inaccessible.

- The abundance ratios and scatter levels, both for the α - and for the neutron-capture elements, are consistent with those predicted in chemical evolution models which reproduce the chemical properties of the Milky Way ([Cescutti & Chiappini 2014](#)), and are therefore a good test to our implementation.

- Our results show that both the chemical yields adopted and the use of a differential enrichment are key factors in the determination of the chemical patterns of the old stars, as well as in their scatter. Despite the fact that changing the sub-grid physics and other numerical aspects might have an effect on our results ([Scannapieco et al. 2012](#)), the tests presented here have shown that the results on the scatter of the different elements is robust.

The success of our implementation in reproducing the scatter levels of the different elements opens up the possibility to study, in a much more realistic manner than possible before, the chemical properties of all old stellar components in galaxies, most notably the bulge, which is the subject of the next paper of this series. In combination with the effects of SNIa and AGB stars, these models have the potential to provide detailed chemical abundances for all components in galaxies, which can be used to put additional constraints on the sub-grid physics describing star formation and feedback, and that are necessary to provide more predictive power to simulations in the Λ CDM cosmology.

ACKNOWLEDGMENTS

CS gratefully acknowledges the Gauss Centre for Supercomputing e.V. (www.gauss-centre.eu) for funding this project by providing computing time on the GCS Supercomputer SuperMUC at Leibniz Supercomputing Centre (www.lrz.de) through project pr49zo, the Leibniz Gemeinschaft for funding this project through grant SAW-2012-AIP-5 129, and the TUPAC supercomputer of CONICET in Argentina, where we have run some of the simulations. CC acknowledges support from DFG Grant CH1188/2-1. GC and CC acknowledge partial support from ChETEC COST Action (CA16117), supported by COST (European Cooperation in Science and Technology).

REFERENCES

- Aguado D. S., et al., 2021, [ApJ](#), **908**, L8
 Belokurov V., Deason A. J., Koposov S. E., Catelan M., Erkal D., Drake A. J., Evans N. W., 2018, [MNRAS](#), **477**, 1472
 Belokurov V., Deason A. J., Erkal D., Koposov S. E., Carballo-Bello J. A., Smith M. C., Jethwa P., Navarrete C., 2019, [MNRAS](#), **488**, L47

- Bertelli G., Bressan A., Chiosi C., Fagotto F., Nasi E., 1994, *A&AS*, **106**, 275
- Brauer K., Ji A. P., Drout M. R., Frebel A., 2020, arXiv e-prints, p. [arXiv:2010.15837](https://arxiv.org/abs/2010.15837)
- Caughlan G. R., Fowler W. A., 1988, *Atomic Data and Nuclear Data Tables*, **40**, 283
- Cayrel R., et al., 2004, *A&A*, **416**, 1117
- Cescutti G., Chiappini C., 2010, *A&A*, **515**, A102
- Cescutti G., Chiappini C., 2014, *A&A*, **565**, A51
- Cescutti G., François P., Matteucci F., Cayrel R., Spite M., 2006, *A&A*, **448**, 557
- Cescutti G., Chiappini C., Hirschi R., Meynet G., Frischknecht U., 2013, *A&A*, **553**, A51
- Cescutti G., Romano D., Matteucci F., Chiappini C., Hirschi R., 2015, *A&A*, **577**, A139
- Chiappini C., 2013, *Astronomische Nachrichten*, **334**, 595
- Chiappini C., Hirschi R., Meynet G., Ekström S., Maeder A., Matteucci F., 2006, *A&A*, **449**, L27
- Chiappini C., Ekström S., Meynet G., Hirschi R., Maeder A., Charbonnel C., 2008, *A&A*, **479**, L9
- Chiappini C., Frischknecht U., Meynet G., Hirschi R., Barbay B., Pignatari M., Decressin T., Maeder A., 2011, *Nature*, **472**, 454
- Choplin A., Hirschi R., Meynet G., Ekström S., Chiappini C., Laird A., 2018, *A&A*, **618**, A133
- Cowan J. J., Sneden C., Lawler J. E., Aprahamian A., Wiescher M., Langanke K., Martínez-Pinedo G., Thielemann F.-K., 2021, *Reviews of Modern Physics*, **93**, 015002
- Cristallo S., Straniero O., Gallino R., Piersanti L., Domínguez I., Lederer M. T., 2009, *ApJ*, **696**, 797
- François P., Matteucci F., Cayrel R., Spite M., Spite F., Chiappini C., 2004, *A&A*, **421**, 613
- François P., et al., 2007, *A&A*, **476**, 935
- Frebel A., 2018, *Annual Review of Nuclear and Particle Science*, **68**, 237
- Frischknecht U., Hirschi R., Thielemann F. K., 2012, *A&A*, **538**, L2
- Frischknecht U., et al., 2016a, *MNRAS*, **456**, 1803
- Frischknecht U., et al., 2016b, *MNRAS*, **456**, 1803
- Gaia Collaboration, Brown A. G. A., et al., 2018, *A&A*, **616**, A1
- Gaia Collaboration, Brown A. G. A., et al., 2021, *A&A*, **650**, C3
- Grevesse N., Asplund M., Sauval A. J., Scott P., 2010, *Ap&SS*, **328**, 179
- Gudin D., et al., 2021, *ApJ*, **908**, 79
- Guidi G., Scannapieco C., Walcher J., Gallazzi A., 2016, *MNRAS*, **462**, 2046
- Gull M., Frebel A., Hinojosa K., Roederer I. U., Ji A. P., Brauer K., 2021, *ApJ*, **912**, 52
- Haynes C. J., Kobayashi C., 2019, *MNRAS*, **483**, 5123
- Helmi A., 2020, *ARA&A*, **58**, 205
- Helmi A., Babusiaux C., Koppelman H. H., Massari D., Veljanoski J., Brown A. G. A., 2018, *Nature*, **563**, 85
- Hirschi R., 2007, *A&A*, **461**, 571
- Kennicutt Jr. R. C., 1998, *ARA&A*, **36**, 189
- Koppelman H. H., Helmi A., Massari D., Roelenga S., Bastian U., 2019, *A&A*, **625**, A5
- Limberg G., et al., 2021, *ApJ*, **913**, L28
- Limongi M., Chieffi A., 2018, *ApJS*, **237**, 13
- Maeder A., Meynet G., 1989, *A&A*, **210**, 155
- Majewski S. R., et al., 2017, *AJ*, **154**, 94
- Meynet G., Maeder A., 2002, *A&A*, **390**, 561
- Miglio A., et al., 2021, *A&A*, **645**, A85
- Montalbán J., et al., 2021, *Nature Astronomy*, **5**, 111
- Montes F., et al., 2007, *ApJ*, **671**, 1685
- Myeong G. C., Vasiliev E., Iorio G., Evans N. W., Belokurov V., 2019, *MNRAS*, **488**, 1235
- Naidu R. P., Conroy C., Bonaca A., Johnson B. D., Ting Y.-S., Caldwell N., Zaritsky D., Cargile P. A., 2020, *ApJ*, **901**, 48
- Naiman J. P., et al., 2018, *MNRAS*, **477**, 1206
- Navarro J. F., White S. D. M., 1993, *MNRAS*, **265**, 271
- Nuza S. E., Parisi F., Scannapieco C., Richter P., Gottlöber S., Steinmetz M., 2014, *MNRAS*, **441**, 2593
- Pignatari M., Gallino R., Meynet G., Hirschi R., Herwig F., Wiescher M., 2008, *ApJ*, **687**, L95
- Poulhazan P.-A., Scannapieco C., Creasey P., 2018, *MNRAS*, **480**, 4817
- Prantzos N., Abia C., Limongi M., Chieffi A., Cristallo S., 2018, *MNRAS*, **476**, 3432
- Raiteri C. M., Villata M., Navarro J. F., 1996, *aap*, **315**, 105
- Re Fiorentin P., Spagna A., Lattanzi M. G., Cignoni M., 2021, *ApJ*, **907**, L16
- Roederer I. U., Preston G. W., Thompson I. B., Shtetman S. A., Sneden C., Burley G. S., Kelson D. D., 2014, *AJ*, **147**, 136
- Roederer I. U., Hattori K., Valluri M., 2018, *AJ*, **156**, 179
- Sawala T., Scannapieco C., Maio U., White S., 2010, *MNRAS*, **402**, 1599
- Sawala T., Guo Q., Scannapieco C., Jenkins A., White S., 2011, *MNRAS*, **413**, 659
- Sawala T., Scannapieco C., White S., 2012, *MNRAS*, **420**, 1714
- Scannapieco C., Tissera P. B., White S. D. M., Springel V., 2005, *MNRAS*, **364**, 552
- Scannapieco C., Tissera P. B., White S. D. M., Springel V., 2006, *MNRAS*, **371**, 1125
- Scannapieco C., Tissera P. B., White S. D. M., Springel V., 2008, *MNRAS*, **389**, 1137
- Scannapieco C., White S. D. M., Springel V., Tissera P. B., 2009, *MNRAS*, **396**, 696 (S09)
- Scannapieco C., Gadotti D. A., Jonsson P., White S. D. M., 2010, *MNRAS*, **407**, L41
- Scannapieco C., White S. D. M., Springel V., Tissera P. B., 2011, *MNRAS*, **417**, 154
- Scannapieco C., et al., 2012, *MNRAS*, **423**, 1726
- Shen S., Cooke R. J., Ramirez-Ruiz E., Madau P., Mayer L., Guedes J., 2015, *ApJ*, **807**, 115
- Sneden C., Cowan J. J., Gallino R., 2008, *ARA&A*, **46**, 241
- Springel V., Hernquist L., 2003, *MNRAS*, **339**, 289
- Springel V., et al., 2008, *MNRAS*, **391**, 1685
- Sutherland R. S., Dopita M. A., 1993, *ApJS*, **88**, 253
- Tissera P. B., Scannapieco C., Beers T. C., Carollo D., 2013, *MNRAS*, **432**, 3391
- Tissera P. B., Beers T. C., Carollo D., Scannapieco C., 2014, *MNRAS*, **439**, 3128
- Valentini M., et al., 2019, *A&A*, **627**, A173
- Wehmeyer B., Pignatari M., Thielemann F. K., 2015, *MNRAS*, **452**, 1970
- Wehmeyer B., Fröhlich C., Côté B., Pignatari M., Thielemann F. K., 2019, *MNRAS*, **487**, 1745
- Woosley S. E., Weaver T. A., 1995, *ApJS*, **101**, 181
- Yong D., et al., 2013, *ApJ*, **762**, 26
- van de Voort F., Quataert E., Hopkins P. F., Kereš D., Faucher-Giguère C.-A., 2015, *MNRAS*, **447**, 140
- van de Voort F., Pakmor R., Grand R. J. J., Springel V., Gómez F. A., Marinacci F., 2020, *MNRAS*, **494**, 4867

APPENDIX A: ADDITIONAL TESTS OF THE CODE

A1 The effects of resolution

In this Section we test the effects of resolution on our results, by comparing simulations using the idealized initial conditions of Section 2.2 and varying the number of particles, N (note that N refers here to the number of particles in one dimension, i.e. the total number of particles of the simulation is $N_{\text{tot}} \sim N^3$). In particular, we compare the runs with $N = 64$ of Section 2.2 (i.e. SE64 and ME64) with identical tests using

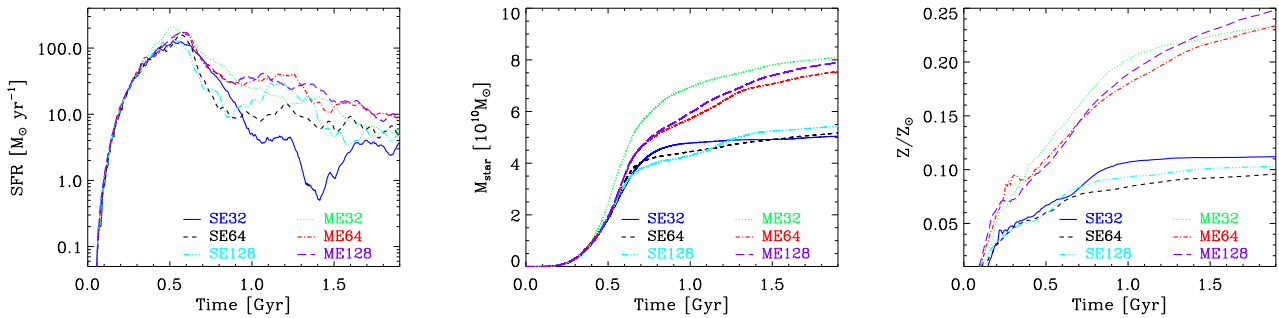


Figure A1. Star formation rates and integrated stellar mass and metallicity as a function of time for our simulations with single/multiple explosion times per SN event and various resolutions.

$N = 32$ and $N = 128$ Following our naming convention used in this work, we refer to the simulations as SE/ME to refer to the single/multiple events per SN explosion, followed by the number N denoting the number of particles. The mass resolution of the simulations with $N = 32, 64$ and 128 is, respectively, $600, 70$ and $9 \times 10^4 M_{\odot}$ for the gas particles and $500, 60$ and $8 \times 10^5 M_{\odot}$ for dark matter particles, and we have used the same gravitational softenings in all runs.

The left- and middle-hand panels of Fig. A1 compare the SFR and cumulative stellar mass as a function of time for our various tests. The runs with $N = 64$ and 128 show very good convergence, particularly at the early times when the star formation activity is at its maximum. In contrast, the lowest resolution runs show somewhat stronger differences. In the SE case, the star formation rate at late times is significantly lower than their counterparts in the runs with higher resolution, although this is not significant in terms of the total stellar mass formed. For ME32, the differences are more important, and appear right at the peak of star formation, producing a noticeable difference, with respect to ME64 and ME128, in the evolution of the stellar mass formed. We note that simulations using multiple events per SN explosion are expected to induce more important differences because the changes in chemical abundance that occur right after the first SN explosions translate into changes in the cooling and the subsequent star formation activity. The faster enrichment in the ME simulations can be observed from the right-hand panel of Fig. A1 where we show the evolution of the total stellar metallicity of our tests with different resolution. After 1 Gyr of evolution, and regardless of resolution, the ME runs have significantly higher metallicities compared to the SE tests.

We have also studied the effects of resolution on the predicted element ratios after 1 Gyr of evolution. As an example, we show in Fig. A2 the results of the ME32, ME64 and ME128 runs, for $[\text{O}/\text{Fe}]$ and $[\text{Ba}/\text{Fe}]$. We find very similar results in all cases, indicating that resolution effects, particularly for $N \geq 64$, are unimportant. Note the very good agreement for the mean/dispersion values, as clearly seen from the right-hand panel of this figure, despite the expected differences in terms of higher resolutions being able to better sample stars at the extremes of the distributions. We conclude that our models are robust against resolution provided 64^3 or more particles are used.

A2 Dependence on number of SPH neighbours

We discuss in this Section the effects of varying the number of SPH neighbours, which determine the spatial extent over which metals are distributed after SN explosion events. This could have an effect on the predicted distributions of chemical abundances through the effects on the mixing of elements in the interstellar medium. In order to investigate this we have run additional tests, both for the SE and ME models, where we increased the number of neighbours from the fiducial value of $N_{\text{ngb}} = 40$ (used in the SE64 and ME64 simulations of Section 2.2) to $64/128$.

Fig. A3 compares the SFR and the evolution of the stellar mass and metallicity for these tests. We find very good convergence of the tests until the peak of the star formation rate, when differences become more significant. In particular, an increase in N_{ngb} translates into an enhancement of star formation activity, which is produced because the chemical elements that are distributed after SN explosions spread over comparatively larger regions. Note that this effect is most clear right after the SF peak, as later on the effects of varying the number of SPH neighbours becomes non trivial: on one hand, the polluted regions are larger enhancing the cooling efficiency and star formation activity, while, on the other, higher SFRs produce larger amounts of feedback that reduce subsequent star formation levels.

Following the behaviour of the SFRs, the total stellar mass formed is in general larger for the simulations with larger N_{ngb} , with more significant differences in the case of the SE runs. A similar behaviour is detected in the case of the stellar metallicities, where differences are more important for the SE runs and not significant for the ME tests. Variations in the stellar metallicity follow the variations in the stellar masses, such that runs with larger N_{ngb} are systematically more enriched.

Finally, we show in Fig. A4 the results of runs with different number of neighbours, for $[\text{O}/\text{Fe}]$ and $[\text{Ba}/\text{Fe}]$ after 1 Gyr of evolution, and their comparison. We find very similar results for both element ratios, indicating that our results are robust against changes in N_{ngb} . Note the excellent agreement of the mean values and also of the scatter, evidenced in the right-hand panel of this figure. We conclude that the results of our model are robust against changes in the number of SPH neighbours used in the simulations.

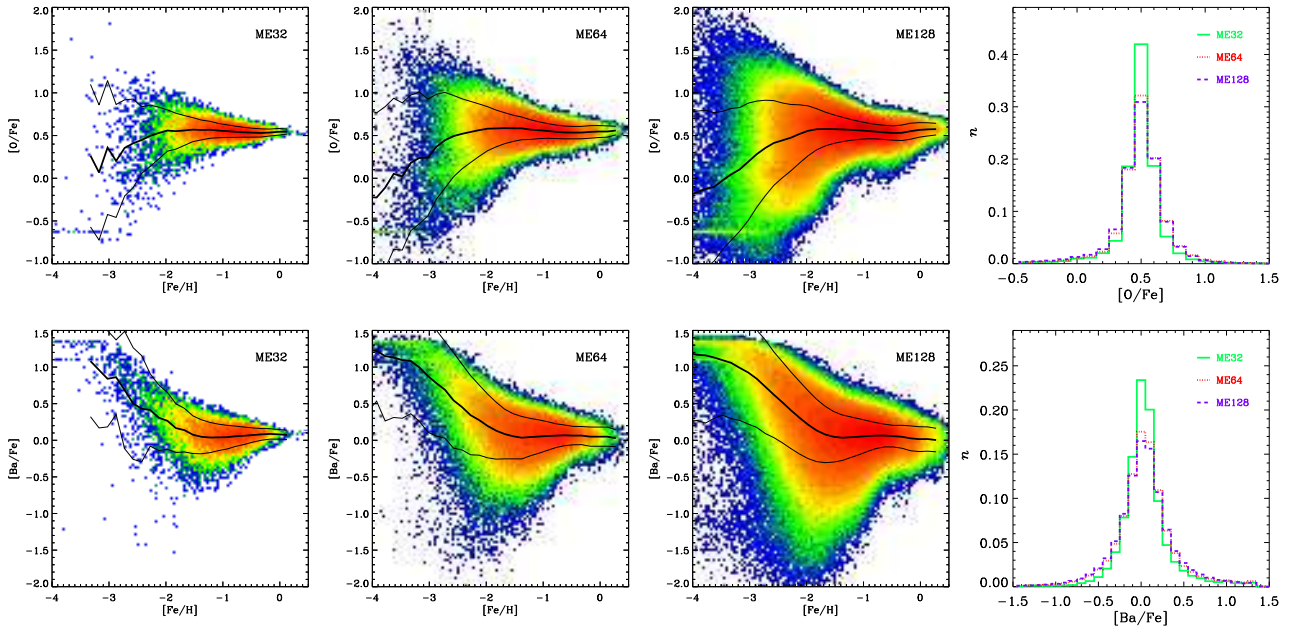


Figure A2. The distribution of $[O/Fe]$ and $[Ba/Fe]$ versus $[Fe/H]$ for our simulations assuming multiple events per SN explosion and different number of particles, after 1 Gyr of evolution. The color scale is normalized to the total number of star particles in each simulation, and we also show the corresponding median (thick lines) and $\pm\sigma$ contours (thin lines). The right-hand panel shows a quantitative comparison of the three distributions.

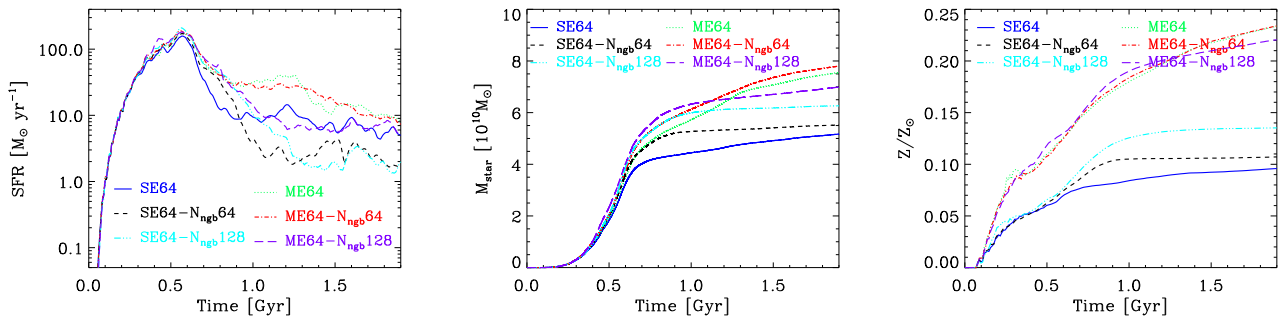


Figure A3. Star formation rates and integrated stellar mass and stellar metallicity as a function of time for our simulations with single/multiple explosion times per SN event and various choices for the number of SPH neighbours.

APPENDIX B: DEPENDENCE OF THE PROPERTIES OF HALO STARS WITH THE AGE THRESHOLD ASSUMED

As discussed throughout this work, the selection of the *stellar halo* stars in the simulations is somehow arbitrary. In this work, we use an age limit of $\tau=1$ Gyr and a radial cut of 5 kpc to define the halo, the last condition is included in order to avoid contamination by the bulge. A variation in τ , particularly in the case it is significantly reduced, might affect some of our results, because the chemical pollution of the interstellar medium changes significantly with time, particularly at the early epochs analyzed in this work. In order to test the dependence of our results to changes in τ , we varied it from the standard value to 0.5 Gyr, 0.3 Gyr and 100 Myr. In this last case, we consider the 100 Myr subsequent to the formation of the first star in the simulation.

We find no significant differences in the abundance ratios and scatter of all elements when the age threshold is changed to 0.5 or 0.3 Gyr; however, some variations appear when we consider the very old stars, as we show below. In Fig. B1 we compare the distribution of the various elements for $\tau = 1$ Gyr (black) and $\tau = 100$ Myr (red). For the α -elements, the effect of reducing τ is a shift toward higher abundances, because enrichment with these elements is faster compared to iron: even though both the α -elements and iron are produced in SNII (recall we ignore SNIa and AGB stars in these simulations) the iron yields are comparatively lower for metal-poor stars. For $\tau = 100$ Myr, the interstellar medium did not yet have time to enrich sufficiently so that the most massive stars produce significant amounts of iron compared to the α -elements. In contrast, for the neutron-capture elements Sr and Ba we find that the

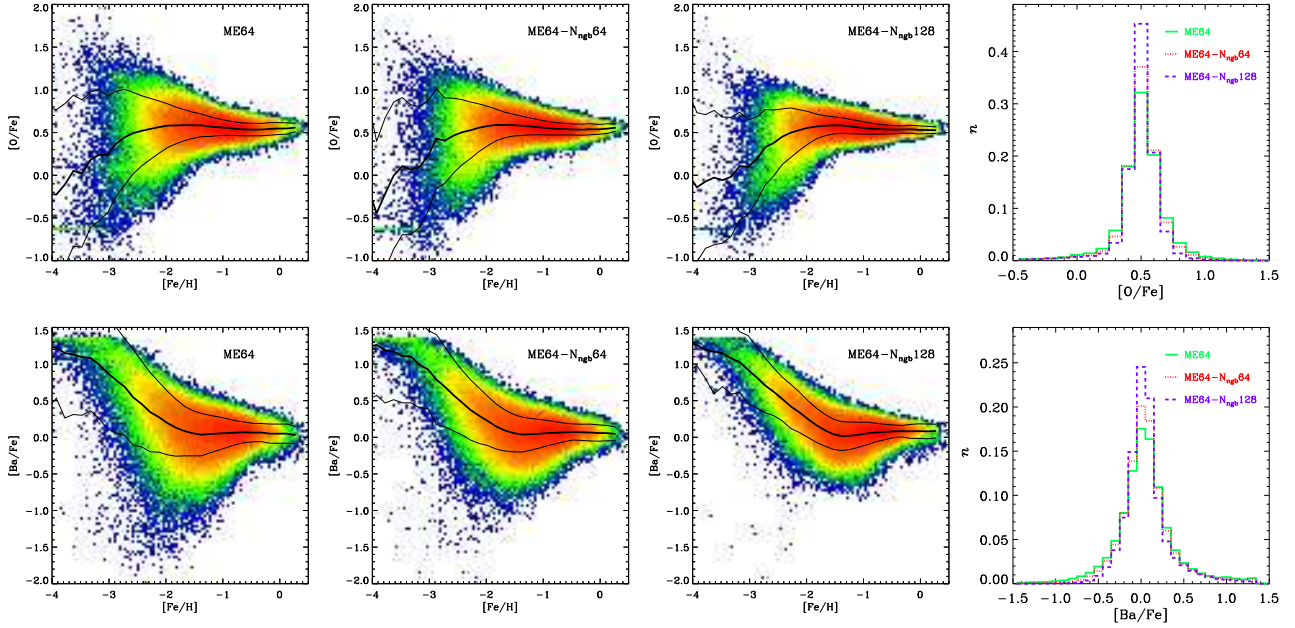


Figure A4. The distribution of $[O/Fe]$ and $[Ba/Fe]$ versus $[Fe/H]$ for our simulations assuming multiple events per SN explosion and different number of SPH neighbours, after 1 Gyr of evolution. The color scale is normalized to the total number of star particles in each simulation, and we also show the corresponding median (thick lines) and $\pm\sigma$ contours (thin lines). The right-hand panel shows a quantitative comparison of the three distributions.

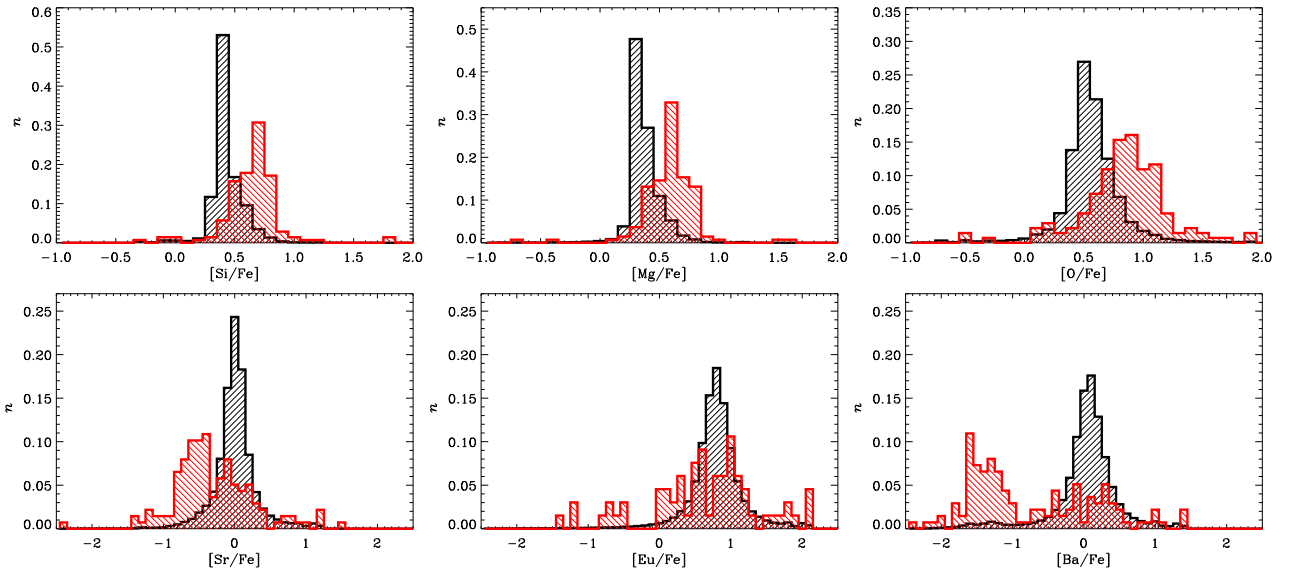


Figure B1. Normalized distribution functions of the various element ratios for halo stars (formed during the first Gyr, black) and the very old stars (formed until 100Myr after the formation of the first stars, red). Note that the various panels have different x -ranges in order to highlight the features of the distributions for different elements.

very old stars have lower abundance ratios compared to the fiducial halo sample, with larger scatter. For Eu, the abundances are similar, but the scatter is also larger when we consider the very old stars. In this case, stars formed from non contaminated gas produce both iron and the neutron-capture elements in the same progenitors, but as the interstellar medium is contaminated enrichment with iron occurs

faster compared to the neutron-capture elements. For this reason, once the very early stages of star formation have completed, the interstellar medium becomes more homogeneous, producing narrower abundance ratio distributions.

Clearly, the different effects of a variation in τ for the abundances of the α - and neutron-capture elements is a manifestation of the masses of their progenitors and the re-

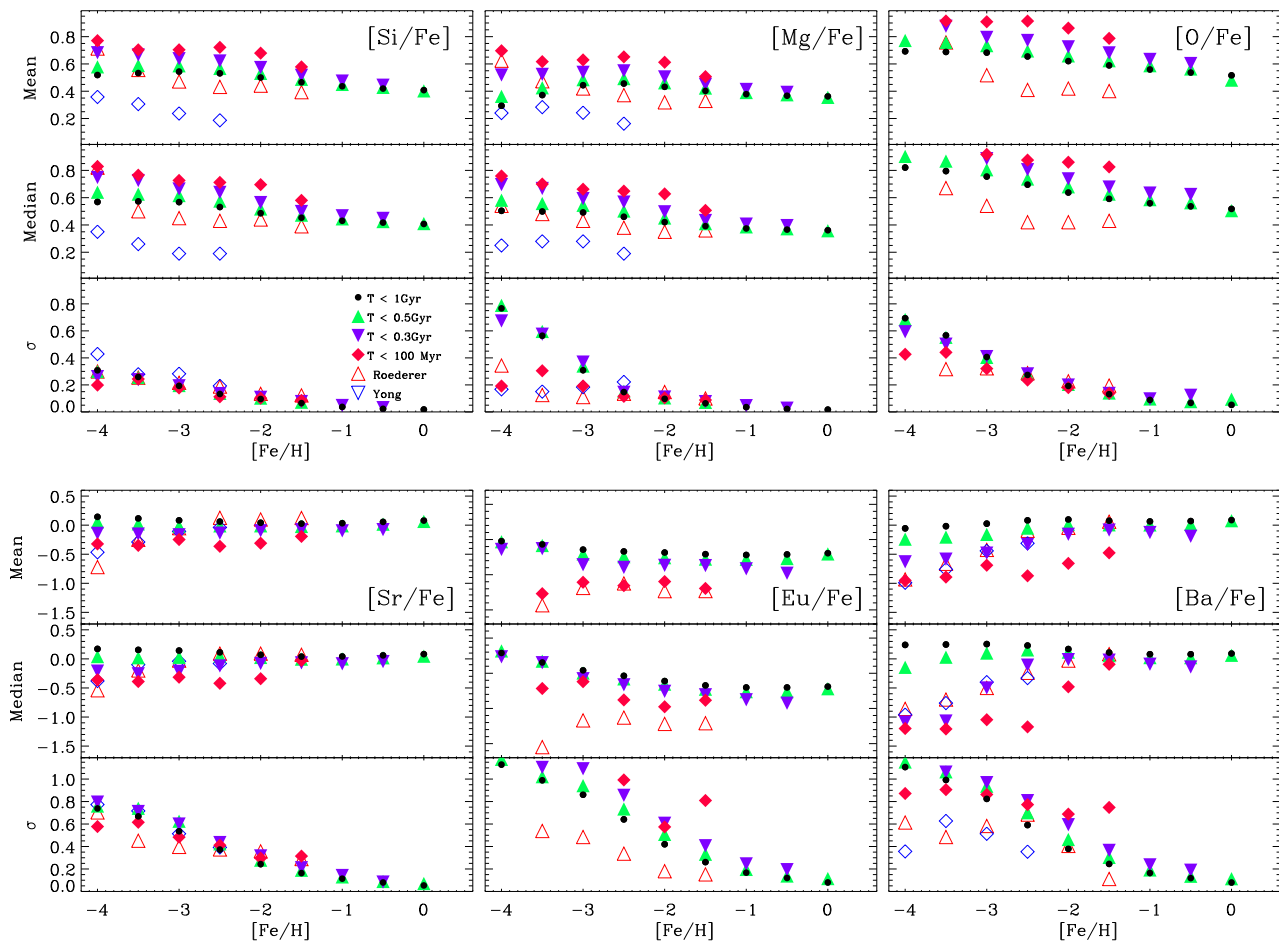


Figure B2. The mean, median and $1 - \sigma$ levels for the different elements, as a function of the iron abundance, for the fiducial stellar halo sample in simulation ME (black). We also include results considering stars with different stellar age ranges, as indicated. The open symbols correspond to the observational data of Roederer et al. 2014 (red triangles) and Yong et al. (blue diamonds).

sulting typical time-scales. In the case of the scatter, considering the very old stars produces wider distributions for all elements, because the interstellar medium is less homogeneous compared to later times.

We also find differences in the distribution functions of [Sr/Ba] when we change the value of τ from 1 Gyr to 100 Myr (with less pronounced differences for $\tau = 0.5$ and 0.3 Gyr).

Finally, we compare in Fig. B2 the mean, median and $1 - \sigma$ values for the different element ratios, as a function of the iron abundance. In this case, we show results for $\tau = 1$ Gyr, 0.5 Gyr, 0.3 Gyr and 100 Myr, and we also include the results for the observational data used in this work: Roederer et al. (2014) and Yong et al. (2013). As we go from the fiducial $\tau = 1$ Gyr to $\tau = 100$ Myr, we find an increase in the mean and median abundances of the α -elements, while the scatter levels do not vary significantly, except for the low [Fe/H] end. Overall, the agreement with the observational data is better for $\tau = 1$ Gyr compared to the lower τ values.

For the neutron-capture elements, reducing τ results in lower mean and median abundance values, with different levels of variations depending on the element. A better agree-

ment with observations is obtained for the smallest τ values in the case of Sr and Eu, but not for Ba. In terms of the scatter, we find very small variations in Sr when τ is varied, and larger but moderate variations for the other neutron-capture elements. The scatter levels of Eu and Ba show the larger disagreement with the observations, with the simulations predicting higher scatter values for all metallicities.

This paper has been typeset from a $\text{\TeX}/\text{\LaTeX}$ file prepared by the author.